Heat Spreader Thermal Switch for Power Converter Isothermalization

Tianyu Yang, Fei Diao, *Graduate Student Member, IEEE*, H. Alan Mantooth, *Fellow, IEEE*, Yue Zhao, *Senior Member, IEEE*, William P. King, *Fellow, IEEE*, and Nenad Miljkovic, *Member, IEEE*

***Abstract*— Power module heat dissipation with spatial inhomogeneity and induced nonuniform temperature distribution presents a challenging concern for system reliability due to thermo-mechanical stresses. These reliability challenges are especially important for nonplanar designs using 3-D packaging principles. Here, we develop a heat spreader thermal switch capable of actively reducing temperature gradients between silicon carbide (SiC) devices in a three-level T-type power converter, which can change depending on electronic operating conditions. The heat spreader thermal switch consists of a stainless-steel (SS) heat spreader and a copper sliding switch embedded within the spreader. Heat transfer from the SiC devices and within the spreader can be controlled by moving the slider between positions within the spreader. To understand heat transfer mechanisms and design the heat spreader thermal switch, we conducted 3-D finite element method simulations to calculate the minimum attainable temperature difference between SiC devices. We used the finite element simulation to quantify the reduction in junction temperature swing during dynamic operation and coupled the results to the Coffin–Manson reliability model to quantify lifetime to failure. We integrated the heat spreader thermal switch with one phase of a three-phase T-type converter and demonstrated isothermalization at different working conditions. At 2.4-kW converter power, each hot SiC device dissipated 4.7 W of heat, resulting in a device case temperature of 43 °C, with each cold SiC device dissipating 1.7 W at 38 °C. The device-to-device temperature difference was decreased from 5 °C to 0 °C by moving the switch a distance of 20 mm. Finite volume method (FVM) simulations of the conjugate heat transfer problem validate the experimental results and support analysis of key performance parameters. This work demonstrates successful isothermalization of a power converter with an active heat spreader thermal switch and develops simulation and design guidelines for successful electro-thermal codesign and implementation of thermal switches for other electronics applications for which isothermalization and enhanced device reliability is a key issue.**

***Index Terms*— Electro-thermal, heat conduction, power electronics, reliability, silicon carbide (SiC), stress, thermal management, wide bandgap.**

Manuscript received 14 September 2021; revised 18 April 2022; accepted 23 May 2022. Date of publication 24 June 2022; date of current version 26 July 2022. This work was supported by the National Science Foundation Engineering Research Center for Power Optimization of Electro-Thermal Systems (POETS) under Cooperative Agreement EEC-1449548. The work of Nenad Miljkovic was supported by the International Institute for Carbon Neutral Energy Research through the Japanese Ministry of Education, Culture, Sports, Science and Technology, under Grant WPI-I2CNER. Recommended for publication by Associate Editor K. Ramakrishna upon evaluation of reviewers' comments. *(Corresponding authors: William P. King; Nenad Miljkovic.)*

Tianyu Yang is with the Department of Mechanical Science and Engineering, University of Illinois at Urbana–Champaign, Urbana, IL 61801 USA.

Fei Diao, H. Alan Mantooth, and Yue Zhao are with the Department of Electrical Engineering, University of Arkansas, Fayetteville, AR 72701 USA.

William P. King is with the Department of Mechanical Science and Engineering, the Department of Materials Science and Engineering, the Materials Research Laboratory, and the Beckman Institute for Advanced Study, University of Illinois at Urbana–Champaign, Urbana, IL 61801 USA (e-mail: wpk@illinois.edu).

Nenad Miljkovic is with the Department of Mechanical Science and Engineering, the Materials Research Laboratory, and the Department of Electrical and Computer Engineering, University of Illinois at Urbana–Champaign, Urbana, IL 61801 USA, and also with the International Institute for Carbon Neutral Energy Research (WPI-I2CNER), Kyushu University, Nishi-ku, Fukuoka 819-0395, Japan (e-mail: nmiljkov@illinois.edu).

Color versions of one or more figures in this article are available at https://doi.org/10.1109/TCPMT.2022.3185972.

Digital Object Identifier 10.1109/TCPMT.2022.3185972

I. Introduction

RELIABILITY constraints of power electronic devices are important concerns for the automotive and aerospace industries due to safety requirements [1], [2]. The main reliability challenges come from high power density products used in extreme temperature applications and transient operation [3]. Reliability issues due to thermo-mechanical stresses contribute to more than 50% of power electronic stress failures. The majority of failure events occur due to the breakdown of fragile semiconductor components and failure of interconnects between dissimilar materials [1], [3]–[5]. A fraction of these failures can be avoided by ensuring proper thermal management and implementing temperature control. Various thermal management methods have been used to manage thermal energy in semiconductor devices [6]–[9]. However, established methods mainly focus on managing junction temperatures and do not focus on reducing cyclic temperature swings or device-to-device temperature gradients. To address thermo-mechanical stress concerns due to cooling constraints, designers typically focus on circuit layout, component location optimization, or engineering thermal pathways [10]–[12]. Other approaches to mitigate thermo-mechanical stress focus on strategies to reduce temperature swings using resistive heaters or tuning drive signals and device heat losses based on feedback from real-time temperature measurements [12]–[18]. For example, doped silicon, silicide, and metalized tungsten resistive heaters have been integrated and used to stabilize chip temperatures using heating compensation [16]. However, on-chip fabrication of microscopic heaters alongside devices is necessary to have instant temperature response [17]–[19].

Moreover, thermal insulation trenches are required to minimize heat leakage. Compared with conventional approaches, a component such as a thermal switch between the converter and heat sink has the potential to be an alternative, passive or active way to reduce temperature gradients or temperature swings.

Thermal switches have been used in cryogenic refrigeration, thermal computing, and spacecraft applications where active control of heat transfer is required [20]–[22]. The thermal switch, analogous to an electrical switch, is used to improve heat transfer when the switch is in the ON state and to reduce heat transfer when the switch is in the OFF state [23]. Different types of thermal switches such as magneto-mechanical, liquid bridge, and variable conductance heat pipes (VCHP) have been developed for various applications using conduction, convection, and radiation heat transfer [24]–[28]. The VCHP can control the thermal conductance of the heat pipe by heating a reservoir of vapor and noncondensable gas [28]. However, the controllability is sensitive to reservoir size, vapor medium characteristics, and ambient temperature. Precise temperature control requires precise, rapid, and active control of reservoir heat input, which undermines applications requiring transient responses at short time scales. Other approaches such as thermoelectric modules have been used to actively control the temperature of electronic components [29]. Their high power consumption, narrow temperature and heat control ranges, and low effective thermal conductivity present challenges for high power density applications having large temperature swings.

Overall, established thermal control methods can be characterized as steady state or long timescale ($\sim$10 s) approaches [29]–[32]. Longer timescale switching is prevalent in many applications. For example, in solar applications, solar inverters show frequent power load oscillations due to the presence of rolling clouds which occur on second or minute timescales [33], [34]. In heavy-duty vehicle applications, load oscillations on long timescales can occur depending on the drive cycle of the vehicle [35].

High-contrast thermal switches formed by enabling motion of a high thermal conductivity medium in a low thermal conductivity channel are promising for active temperature control in high-power transient applications [23], [36]. However, published research on such thermal switches mostly focuses on controlling heat transfer at the micrometer to nanometer scale. The relatively small size of previous thermal switches prevents their use with power electronic devices which have relatively large active components (mm to cm scale). A need exists to develop cm-scale thermal switches that can be used for power converter applications that require passive or active heat transfer control to reduce device-to-device temperature gradients or temperature swings.

Here, we develop a heat spreader thermal switch consisting of a stainless steel (SS) heat spreader and a copper (Cu) thermal switch. We evaluate the thermal control performance on a T-type power converter using silicon carbide (SiC) power metal–oxide–semiconductor field-effect transistors (MOSFETs). Efficient heat transfer through the Cu switch reduces junction-to-coolant thermal resistance from hot SiC devices. Meanwhile, the air channel within the SS spreader blocks heat transfer and increases the junction-to-coolant thermal resistance from cold SiC devices. The SS heat spreader with relatively low thermal conductivity confines the lateral heat transfer and enhances the temperature controllability through the Cu switch. In the static operational mode, the thermal switch is designed to isothermalize SiC devices by improving heat transfer from hot SiC devices and reducing heat transfer from cold SiC devices. In the dynamic operational mode, enabled by moving the thermal switch dynamically in the heat spreader channel, we show that manipulating the heat transfer reduces temperature swings and enhances reliability of SiC devices. Section II presents the thermal switch concept and design to isothermalize SiC devices of a dc/ac power converter and reduce temperature swings for enhanced reliability. Dimensions and materials of the thermal switch are analyzed to quantify enhanced performance. Section III shows the experiment methodology and heat transfer analysis. Section IV discusses the experiment and simulation results, as well as discusses applications. Section V provides conclusions for this article.

II. Concept and Design

A. Thermal Switch Concept and Integration With a Power Converter

Fig. 1 shows the concept of the solid heat spreader thermal switch integrated with two discrete SiC devices (SiC1 and SiC2) connected to the converter printed circuit board (PCB). The solid heat spreader thermal switch consists of an SS heat spreader and a Cu thermal switch that can move along the air channel embedded in the SS spreader. The heat spreader is constructed of SS 304 material [$k_{SS} = 15.9$ W/(m·K)], which is rationally selected as the spreader material to confine the lateral heat transfer and enhance the temperature controllability of the thermal switch when the spreader conducts heat losses Q_1 and Q_2 from SiC1 and SiC2 to the thermal switch. When the thermal switch is integrated symmetrically with the SiC devices, as shown in Fig. 1(a), heat losses ($Q_1 > Q_2$) are transferred to the aluminum (Al) heat sink efficiently, which leads to junction temperature differences between SiC1 and SiC2 ($T_{j,1} > T_{j,2}$). To reduce the temperature difference, the Cu thermal switch is moved closer to hot SiC1 device by a distance defined as x in Fig. 1(b). The Cu thermal switch with thermal conductivity of $k_{Cu} = 385$ W/(m·K) improves heat conduction from hot SiC1 device, while the low thermal conductivity air [$k_{Air} = 0.024$ W/(m·K)] beneath the cold SiC2 device residing in the SS channel reduces heat conduction. By moving the thermal switch to a specific position designed for specified working conditions of the converter, the SiC junction temperature difference can be eliminated.

The solid heat spreader developed here is tailored to isothermalize a three-level (3-L) T-type power converter. Fig. 2(a) shows the circuit topology of the power converter. The 3-L T-type converter is widely used in low- or medium-voltage applications and has advantages over other two-level converters such as simple operation, lower conduction and switching losses, and superior converter output voltage quality

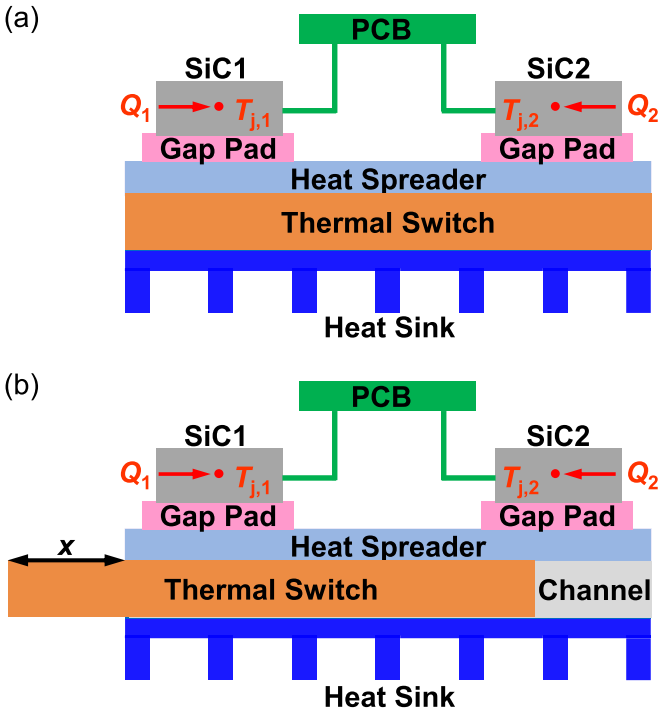

Fig. 1. Schematic of the solid heat spreader thermal switch integrated with two SiC devices when Cu thermal switch (a) resides in the air channel and (b) is moved to position x along the channel. Devices SiC1 and SiC2 dissipate Q_1 and Q_2, respectively ($Q_1 > Q_2$), which results in junction temperature difference ($T_{j,1} > T_{j,2}$) for the condition depicted in (a). The SS heat spreader spreads heat from SiC devices to Cu thermal switch. The thermal switch can be moved within the air channel embedded in the SS spreader to transfer heat more efficiently from SiC1 and less efficiently from SiC2 as depicted in (b) to isothermalize SiC1 and SiC2 ($T_{j,1} = T_{j,2}$). Once spread through SS spreader and Cu switch, heat is dissipated to a coolant via a heat sink.

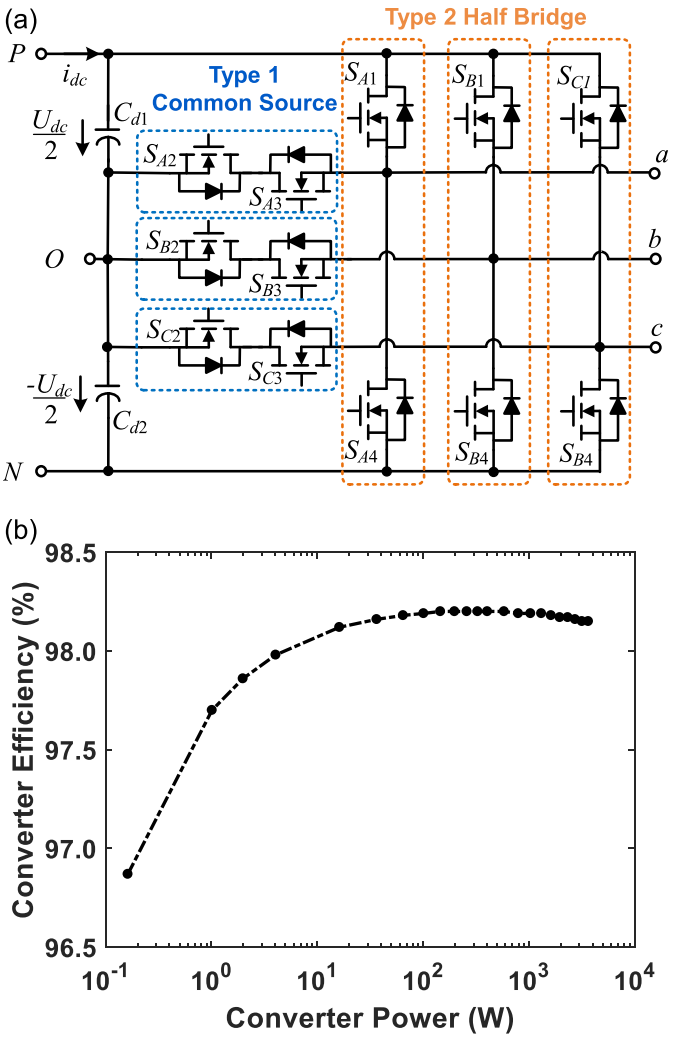

Fig. 2. (a) Schematic of the three-level T-type converter topology. Cold SiC devices in type 1 CS dissipate less heat than hot SiC devices in type 2 HB due to their lower voltage load and switching frequency. (b) Efficiency of the T-type converter as a function of operating power with a unity power factor load and 20-kHz switching frequency at 25 °C.

[37], [38]. The SiC MOSFETs, used in high power density, high-efficiency power converters applications such as solar inverter and motor drives [38], [39], are used as demonstration devices. Each phase of the converter has four SiC devices (C2M0160120D, Cree) shown in Fig. 2(a). Two of the devices form a common-source (CS) configuration (Type 1), while the other two form a half-bridge (HB) configuration (Type 2). Hot SiC devices in the HB configuration withstand the full dc bus voltage, while cold SiC devices in the CS configuration only block half of the dc bus voltage. In addition, the operating conditions such as switching frequency of these two configurations are different, leading to different device heat losses $Q_1 > Q_2$, as depicted in Fig. 1. The different heat losses result in different junction temperatures between the SiC devices when cooled by a homogeneous heat sink without thermal switch integration. Fig. 2(b) shows the converter efficiency as a function of converter power when the converter works at unity power factor. The heat losses of all the components are calculated to obtain the converter efficiency using a precise circuit loss model [38]. The calculated peak efficiency is 98.2% when the converter works beyond 0.6 kW. The circuit topology and heat loss calculations provide a way to obtain heat losses Q_1 and Q_2 of hot SiCs and cold SiCs when the power converter works at different powers and temperatures in our experiments.

B. Thermal Switch Design for Isothermalization

To design the heat spreader thermal switch, we used 3-D FEM simulations in COMSOL Multiphysics 5.4.0. Fig. 3 shows the temperature predictions of the integrated heat spreader thermal switch with four SiC devices on one phase of the 3-L T-type converter. The heat spreader had dimensions of 107 mm × 100 mm × 10 mm with 1-mm-thick spreader and 9-mm-thick air channel, and the thermal switch had dimensions of 107 mm × 80 mm × 9 mm, designed according to converter size requirement. The 3-D FEM model was built to study the thermal performance of the switch when the converter worked at different conditions. Temperature-dependent heat losses Q_1 and Q_2 from hot and cold SiC devices were obtained from a precise circuit model [38] and were modeled as volumetric heat sources in FEM thermal simulations. The heat sink beneath the thermal switch was cooled by air at temperature $T_{\text{air}} = 25$ °C with an effective spatially averaged forced convection heat transfer

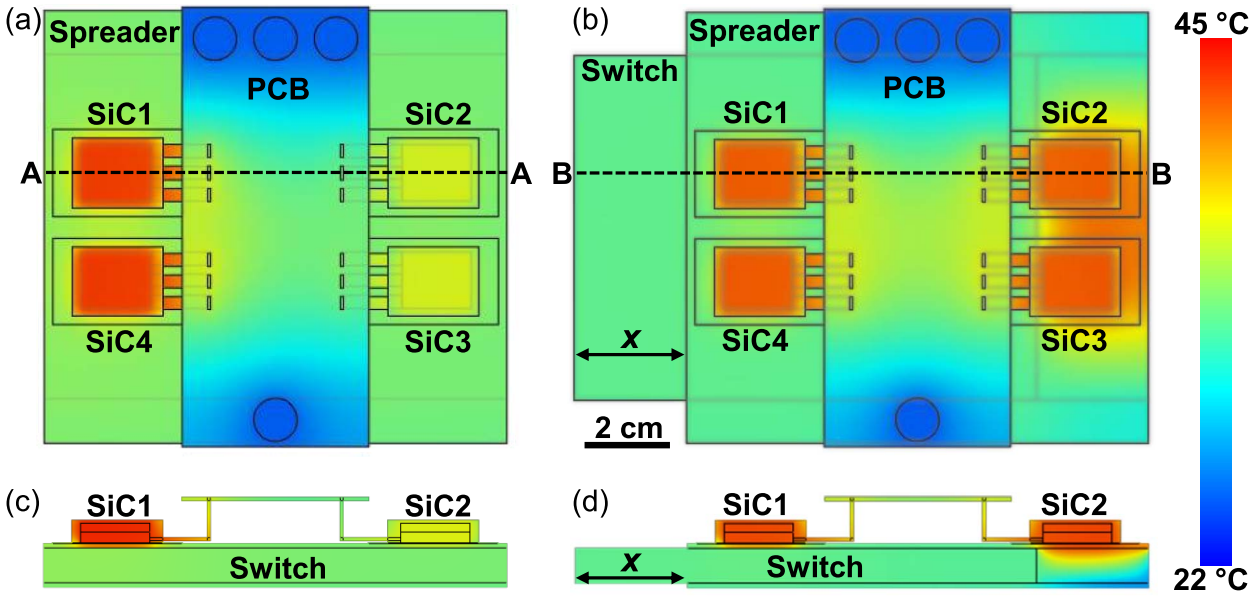

Fig. 3. Top-view temperature distributions of the power converter single phase integrated with the thermal switch obtained from 3-D FEM simulations when the thermal switch resides in the channel at (a) $x = 0$ and (b) $x = 27$ mm. When the thermal switch moves from $x = 0$ to 27 mm, the hot SiC devices (SiC1 and SiC4) decrease slightly in temperature due to more heat spreading from the thermal switch. However, the cold SiC devices (SiC2 and SiC3) increase in temperature due to larger thermal impedance resulting from the SS air channel. The simulation assumes a converter power of 2.4 kW with hot SiC devices dissipating $Q_1 = 4.7$ W and cold SiC devices dissipating $Q_2 = 1.7$ W. Side-view temperature distribution of cross sections (c) A-A and (d) B-B. The air-side heat sink is not shown for clarity.

coefficient of $h = 100$ W/(m^2·K) as the bottom boundary condition [40]. Using the equivalent heat transfer coefficient on the projected boundary area of the heat sink, we matched the thermal conductance between the finned and no-fin heat sinks and fins were not included in following FEM model for computational simplicity. The black-anodized Al heat sink (394-2AB, Wakefield-Vette) has a thermal conductivity of $k_{Al} = 220$ W/(m·K), with a 5-mm-thick base, and 2 fins/in that are 1.5-mm thick and 33-mm long to provide sufficient heat spreading for efficient air cooling. Other surfaces of the integrated assembly were assumed to undergo natural convection with the surrounding air with a spatially averaged heat transfer coefficient of 10 W/(m^2·K). The thermal contact resistance between the heat spreader and the thermal switch was estimated to be 500 (mm^2·K)/W based on the 300-μm-thick gap on each side filled with silicone oil lubricant having a thermal conductivity of 0.6 W/(m·K) [41]. The surface roughness and contact pressure can play a role in thermal contact resistance. Here, we polished the contact surfaces to ensure that roughness is less than the micrometer scale and applied enough lubricant to fill the gap for sliding motion with minimal friction of the switch. The thermal impedance between the SiC device and the heat spreader was simulated by the 150-μm-thick silicone pad which has a thermal conductivity of 0.9 W/(m·K) [42]. The Kapton-reinforced silicone pad was necessary as an electrical insulation medium. Hot SiC devices (SiC1 and SiC4) were simulated as volumetrically distributed heat sources with the same high heat loss, whereas cold SiC devices (SiC2 and SiC3) were heat sources with the same low heat loss. A fine mesh with high element quality was generated and grid independence was checked. For example, when the Cu switch was in the spreader channel symmetrically without movement, a mesh with 228 223 elements was generated with a 0.63 skewness. A nonlinear solver solved for the steady-state temperature distribution with convergence after four iterations and a residual of $<4 \times 10^{-5}$. The grid independence was checked using two finer meshes with 724 988 and 2 680 326 elements, showing maximum temperatures of 43.94 °C and 43.96 °C, with variances of <0.1 °C compared with 43.86 °C using the coarse mesh. For the preliminary design of the heat spreader thermal switch, heat transfer of the single phase was assumed to be independent of the other two phases of the converter. When the thermal switch was placed symmetrically in the spreader channel at position $x = 0$, hot SiC1 and SiC4 had maximum case temperatures of 44 °C, higher than the 37 °C case temperatures of cold SiC2 and SiC3, as shown in Fig. 3(a). To minimize the temperature difference of 7 °C, the thermal switch was moved along the spreader channel to $x = 27$ mm. Actuation approaches such as electrical, pneumatic, hydraulic, magnetic, or electro-mechanical can be used to move the switch in the spreader channel while the spreader is fixed with the power converter. Improved heat conduction from hot SiC1 and SiC4 devices as well as reduced heat conduction from cold SiC2 and SiC3 devices resulted in isothermalization between the devices, which all approached 44 °C [see Fig. 3(b)]. The side-view temperature profiles shown in Fig. 3(c) and (d) revealed that the temperature gradient in the Cu thermal switch was significantly smaller than that of the SS air channel. The change in temperature gradients indicated how the thermal switch manipulated heat transfer pathways from SiC devices to the heat sink. The temperature predictions of FEM simulations

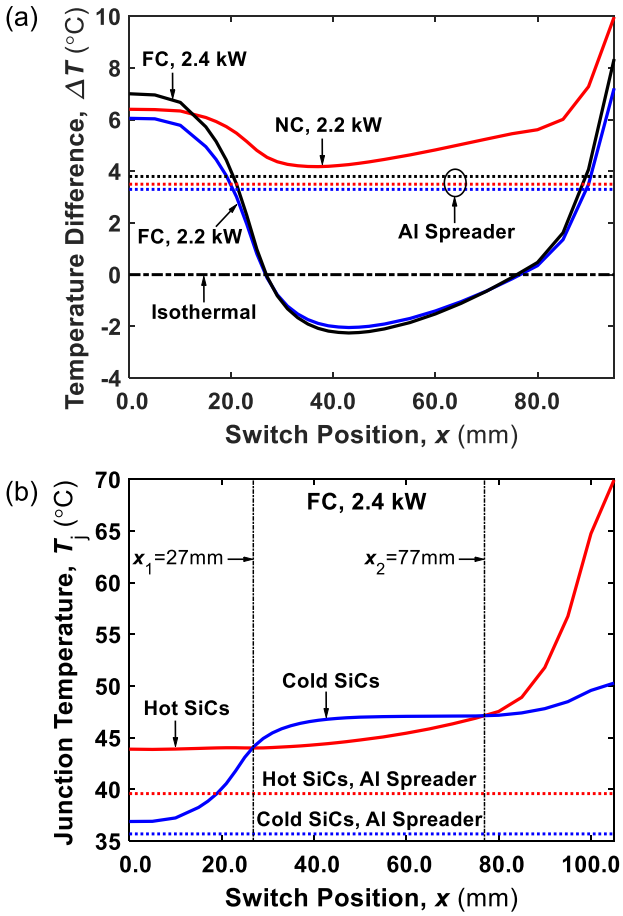

Fig. 4. (a) Three-dimensional FEM simulation results showing SiC device temperature difference ($\Delta T = T_{hot} - T_{cold}$) as a function of switch position (x) when the converter operates at different powers, where T_{hot} and T_{cold} represent the average junction temperatures of hot SiC devices (SiC1 and SiC4) and cold SiC devices (SiC2 and SiC3), respectively. Solid lines represent trend lines. Dotted lines represent the temperature difference present with a solid Al spreader and heat sink. (b) Absolute temperatures of hot and cold SiC devices as a function of switch position (x) when the power converter operates at 2.4 kW cooled by forced convection of ambient air. The results were obtained with 3-D FEM simulations. The switch position $x = 0$ is shown in Fig. 3(a), and represents the case when the Cu block resides symmetrically under SiC devices with the spreader channel filled with Cu switch.

show that the solid heat spreader thermal switch design is capable of eliminating temperature differences between SiC devices by moving the Cu thermal switch to a specific position.

With an emphasis on device-to-device isothermalization by the heat spreader thermal switch, different working conditions of the power converter were next simulated to study whether isothermalization was dependent on Cu switch position (x). Fig. 4(a) shows the FEM simulation results of the temperature difference between hot and cold SiC devices as a function of thermal switch position (x). The temperature difference was defined as $\Delta T = T_{hot} - T_{cold}$, where T_{hot} and T_{cold} represent the average maximum junction temperatures of hot SiC devices (SiC1 and SiC4) and cold SiC devices (SiC2 and SiC3), respectively. Hot SiC devices SiC1 and SiC4 operate at the same conditions with approximate junction temperatures, while cold SiC devices SiC2 and SiC3 operate at the same conditions with approximate junction temperatures. When the power converter operated at 2.4 kW, and the heat sink was cooled by air forced convection, ΔT decreased from 7 °C to 0 °C by moving the thermal switch to $x = 27$ mm. The temperature difference was eliminated due to improved heat conduction from hot SiC devices and reduced heat conduction from cold SiC devices through the heat spreader thermal switch to the heat sink. Moving the thermal switch beyond the optimum point ($x > 27$ mm) resulted in a negative temperature difference, indicating that the less efficient heat transfer from cold SiC devices (SiC2 and SiC3) through the air channel increased T_{cold} to exceed T_{hot}. The trends of T_{cold} and T_{hot} are shown in Fig. 4(b). However, ΔT showed a local minimum at $x = 43$ mm, becoming positive at $x > 77$ mm due to the less efficient heat transfer from hot SiC devices (SiC1 and SiC4). The first isothermal position at $x_1 = 27$ mm was preferred for experimental testing when compared with the second ($x_2 = 77$ mm), since SiC devices were 3 °C colder due to more heat spreading from the thermal switch shown in Fig. 4(b). When the thermal switch moved beyond 30 mm, the majority of heat loss from cold SiC devices transferred through the spreader, device surfaces, leads, and PCB by natural convection instead of the thermal switch. Therefore, switch movement beyond 30 mm did not significantly affect heat transfer and junction temperatures of cold SiC devices. Moreover, FEM simulations with a solid Al spreader having the same dimensions as our heat spreader thermal switch were conducted as a reference. The simulation results show that heat spreading through the Al spreader was sufficient and addition of thickness caused negligible temperature changes. Compared with an Al spreader, the heat spreader thermal switch eliminated the temperature difference at a penalty of increasing the junction temperature by 4 °C.

To understand how the converter power level affects device isothermalization, we simulated a second case where the power converter operated at 2.2 kW. The simulations showed similar trends of temperature difference due to similar heat transfer mechanisms [see Fig. 4(a)]. Interestingly, FEM simulations showed that when the converter was cooled by natural convection of air using the same heat spreader with heat sink and a convective heat transfer coefficient of 10 W/(m^2·K) instead of 100 W/(m^2·K), the temperature difference could not be eliminated by moving the thermal switch. The reason for the loss of temperature control using the thermal switch is due to increased heat transfer from top-side natural convection and reduced heat transfer through the thermal switch itself, limiting the impact of Cu position on SiC junction temperatures. The presence of forced convection on the back side ensures that the majority of heat losses are conducted through thermal switch, resulting in enhanced device temperature control. The results indicate that the developed thermal switch operates with higher efficacy when the thermal resistance from junction to coolant (through the switch) is minimized, and parasitic losses away from the switch are eliminated. For the 2.2-kW converter power case, the temperature difference was minimized to 4.2 °C when the thermal switch was at $x = 37$ mm. To benchmark our thermal switch results to a conventional solution (solid heat sink with no switch), we conducted additional

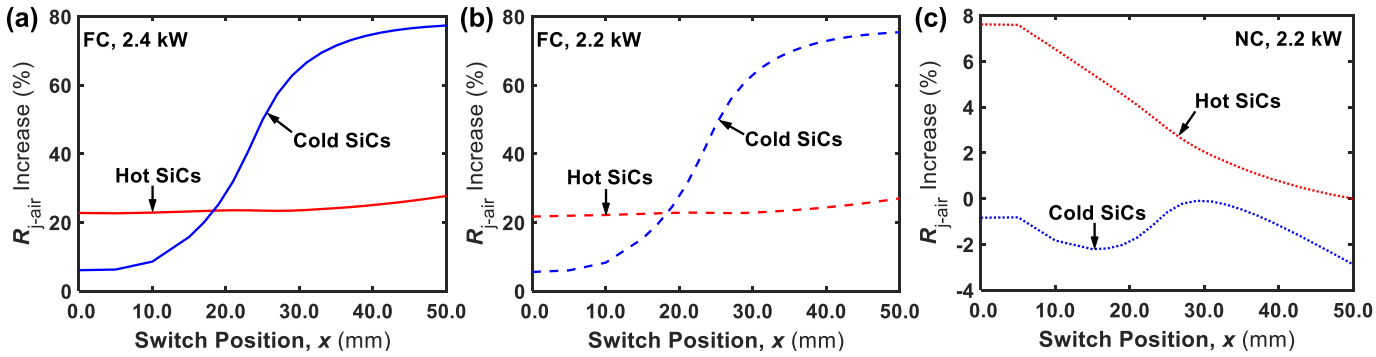

Fig. 5. FEM simulation results showing the total thermal resistance ($R_{j-\text{air}} = (T_j - T_{\text{air}})/Q$) as a function of switch position (x) when the converter operates at (a) 2.4 kW cooled by air forced convection, (b) 2.2 kW cooled by air forced convection, and (c) 2.2 kW cooled by air natural convection.

FEM simulations for a solid Al heat sink. The FEM results show that although an all-Al heat sink results in lower device case temperatures [see Fig. 4(b)], the temperature difference between hot and cold SiC devices ranges from 3.3 °C to 3.8 °C [see Fig. 4(a)]. Larger temperature differences (>10 °C) are expected when the power converter operates at higher powers (>5 kW) and generates more heat loss. The solid Al heat sink results point to the need for integration of a thermal switch to manipulate heat transfer and achieve device-to-device isothermalization.

To explore and demonstrate thermal switch controllability of heat transfer pathways, we analyzed the thermal resistance ($R_{j-\text{air}}$) from the junction to ambient air when the thermal switch moved to different positions. Fig. 5 shows the increase in $R_{j-\text{air}}$ of hot SiC devices (hot SiCs) and cold SiC devices (cold SiCs) as a function of the switch position with the converter operating at different conditions. $R_{j-\text{air}}$ was calculated by computing $(T_{\text{hot}} - T_{\text{air}})/Q_1$ for hot SiCs and $(T_{\text{cold}} - T_{\text{air}})/Q_2$ for cold SiCs. The increase percentage of $R_{j-\text{air}}$ from the thermal switch compared with the all-aluminum heat sink was evaluated by $(R_{j-\text{air,Switch}} - R_{j-\text{air,Al ref}})/R_{j-\text{air,Al ref}}$. When the heat sink was cooled by air forced convection, $R_{j-\text{air}}$ of cold SiCs was increased by 6%–77% depending on the switch position, while $R_{j-\text{air}}$ of hot SiCs was increased by approximately 23% as shown in Fig. 5(a). The majority of the thermal resistance increase in hot SiCs is from the electrical insulation pad and the switching lubricant, which is approximately 15 times higher than the spreader thermal resistance. At the lower power level of 2.2 kW with forced air cooling, the increase in $R_{j-\text{air}}$ [see Fig. 5(b)] showed similar variance as a function of switch position. For natural convection cooling [see Fig. 5(c)], $R_{j-\text{air}}$ of cold SiCs decreased slightly by the presence of the thermal switch due to added surface area undergoing natural convection. The small increase in $R_{j-\text{air}}$ for hot SiCs was due to the gap resistance between the thermal switch and heat spreader as well as heat spreading through the thermal switch, which changed as a function of switch position. The thermal resistance analysis indicates that the thermal switch allows for greater control of cold SiC thermal resistance compared with hot SiC when the heat sink undergoes forced convection with air. However, when natural convection is used, the controllability of the thermal resistance for both hot and cold SiCs becomes negligible due to increased natural convection resistance and significant heat losses to the top side of the converter.

Furthermore, FEM simulations point to the need for rational selection of the thermal switch spreader material to enable device-to-device temperature control. Although utilization of a homogeneous high thermal conductivity heat sink reduces both device-to-device temperature difference and absolute junction temperature, it fails to eliminate or provide any control of device-to-device temperature difference. Indeed, past studies have shown that static temperature gradients and cyclic temperature swings can be key failure points for devices operating in the field for years [2], [43], demonstrating the need for thermal switching and careful selection of the heat spreader material. In our case, SS was chosen due to its ability to limit lateral conduction from hot to cold SiC devices and better parallelize the heat flow patch from the device junction to the coolant on the back side. Similarly, the thin heat spreader with 1-mm thickness was designed to reduce lateral heat spreading from SiC devices and enhance normal heat transfer to the thermal switch. In essence, our heat spreader is a poor spreader by design to enable temperature control.

Fig. 6 shows the FEM simulation results of spreader effects on thermal switch performance when the converter operated at 2.4 kW with air forced convection. Here, we investigated thermal conductivity (k) and thickness (d) of the heat spreader. The effect of three 1-mm-thick spreaders with thermal conductivities of $k = 4$, 40, and 220 W/(m·K) on SiC junction temperatures as a function of switch position was explored in Fig. 6(a). The poor spreader increased temperatures of both hot and cold SiC devices, meanwhile, provided an opportunity to isothermalize SiC devices when the thermal switch was moved to 25 or 80 mm. However, the spreader with a highest thermal conductivity showed negligible controllability of device temperatures when moving the thermal switch. The spreader with a mediate thermal conductivity had advantages of both decreased absolute temperatures and minimum temperature difference. The minimum temperature difference ΔT indicates the heat spreader controllability of hot and cold SiC devices. The achievable minimum temperature difference ΔT as a function of the spreader thermal conductivity is shown in Fig. 6(b). The minimum ΔT increased with spreader thermal

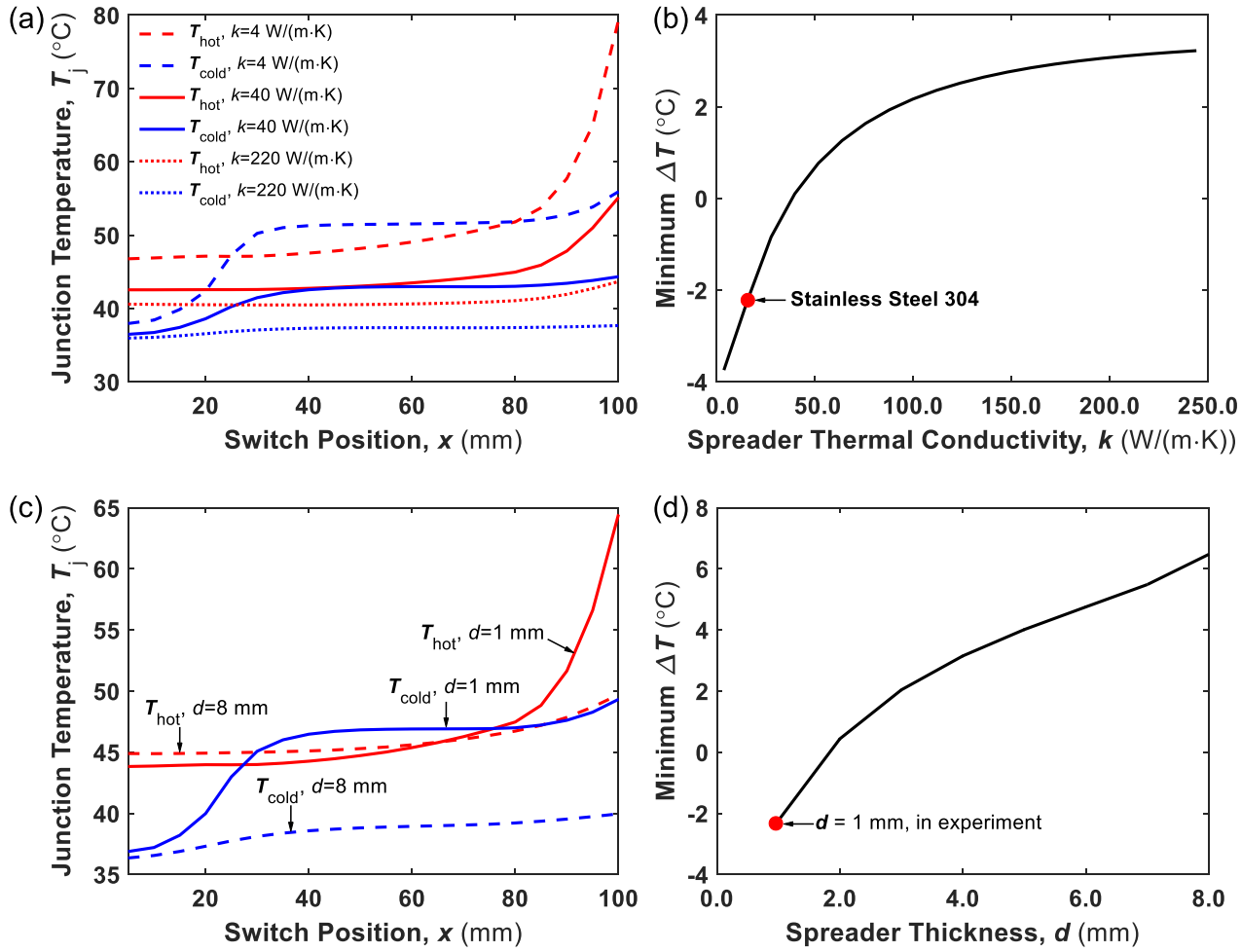

Fig. 6. Effects of heat spreader parameters on thermal switch performance. (a) SiC junction temperatures T_j and (b) minimum achievable temperature difference ΔT as a function of the spreader thermal conductivity, k. (c) SiC junction temperatures T_j and (d) minimum achievable temperature difference ΔT as a function of spreader thickness, d. Simulations used converter power of 2.4 kW with forced convection air cooling.

conductivity due to enhanced lateral heat spreading from hot SiC devices to cold SiC devices. Lower minimum ΔT implies better capability of the heat spreader to increase T_{cold} and decrease T_{hot}, which thus ensures better tolerance to achieve isothermalization by moving the thermal switch. SS 304 was chosen as the spreader material not only to decrease absolute device temperatures but also to provide a tolerance of −2.3 °C minimum ΔT for experiments. Moreover, the effect of the SS 304 spreader thickness on temperatures of hot and cold SiC devices is shown in Fig. 6(c). The use of a thicker spreader ($d = 8$ mm) hindered temperature controllability by stemming normal heat transfer and enhancing lateral heat spreading through a broader lateral area, compared with our thin spreader ($d = 1$ mm). Fig. 6(d) shows the trend of achievable minimum ΔT increasing with the spreader thickness. Our SS heat spreader was designed to be 1-mm thick considering both minimum ΔT and easiness of manufacturing.

In addition to device-to-device isothermalization which is important to reduce temperature gradients and stresses at the system level [12], [44], [45], other package-related failure concerns caused by static or cyclic thermal stresses within individual devices exist, such as bond wire fatigue, liftoff, and chip cracking due to bending stress in the base plate [5]. To investigate the reliability benefit of individual SiC devices from the achieved thermal switch isothermalization, we investigated the static temperature gradient reduction within devices, between devices and their substrates, and within the heat sink. Fig. 7(a) shows the temperature images with isothermal contours of the SiC2 device and the substrate when the device dissipated 1.7 W and the substrate was cooled by forced air convection [$h = 100$ W/(m^2·K)] or liquid convection [$h = 1000$ W/(m^2·K)] at different switch positions. The temperature interval between isothermal contours indicated by white curves was 0.5 °C. When the thermal switch experienced air cooling at the bottom, the switch position to achieve SiC1–SiC2 isothermalization was $x = 27$ mm. However, when using liquid cooling with a 10× higher heat transfer coefficient, the switch position for isothermalization was $x = 23.5$ mm. Even though moving the thermal switch to isothermal positions increased the absolute temperatures of SiC2, the temperature gradients between device and heat spreader substrate and near device corners where three dissimilar materials interconnected (indicated by the black ellipse) were significantly reduced when compared with the baseline positions ($x = 0$ mm).

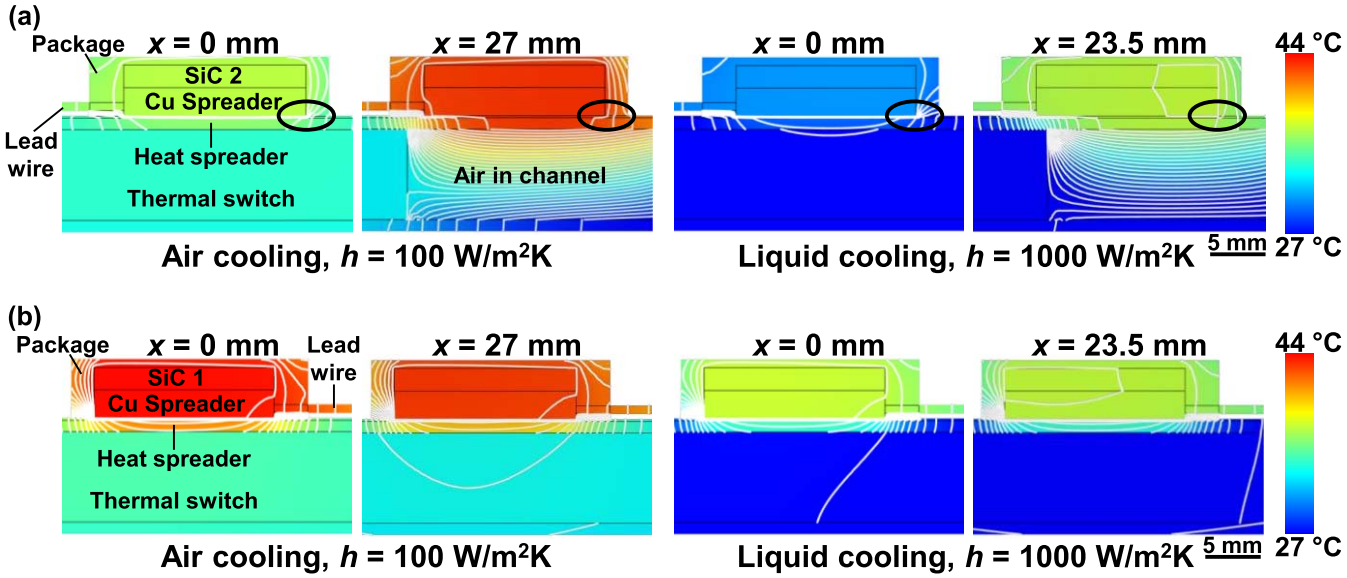

Fig. 7. Temperature distribution with gradients marked at (a) SiC2 and (b) SiC1 devices and substrate when the thermal switch was in its baseline position ($x = 0$ mm) and isothermal positions of $x = 27$ mm for air cooling and $x = 23.5$ mm for liquid cooling. The white contours represent isothermal lines with a temperature interval of 0.5 °C. The black ellipse indicates the most probable failure area where three dissimilar materials of the device, package, and substrate interconnect.

The less effective thermal transport of the heat spreader and air in the channel reduced the temperature gradients and thermo-mechanical stress between the device and the substrate. Moving the thermal switch increased the temperature gradients only slightly in the direction of lead wires. In the heat spreader air channel, the temperature gradients were increased with the thermal switch away from SiC2 device. Fig. 7(b) shows the thermal images and temperature gradients for SiC1 device. The thermal switch at the isothermalization position increased the convection cooling area of the switch and decreased SiC1 junction temperatures slightly by <1 °C. However, temperature gradients in SiC1 were not reduced. The analysis demonstrates that temperature gradients in select locations can be reduced with the thermal switch, which presents a pathway for enhancing reliability.

C. Junction Temperature Swing Reduction Enabled by Static or Dynamic Thermal Switch Operation

Temperature cycling of dissimilar materials with different thermal expansion coefficients is one of the major factors leading to power semiconductor failure. For IGBT modules, a major failure mechanism arising from temperature cycling includes bond wire liftoff and solder joint cracking under the chip and under the ceramic substrate. Both the Coffin–Manson model and Arrhenius model indicate that reducing the cyclic temperature swing improves device lifetime [46]. The cyclic temperature swing results from periodic current communication during SiC switching transition or the converter loading changes. Our converter generated a 60-Hz output voltage with a 20-kHz switching frequency of the SiC devices. During switching transition without converter loading changes, the heat losses changed on the timescale of μs with a period of 17 ms. The thermal penetration depth within 0.01 s is <0.1 mm [41], which is small due to the low thermal conductivity [0.27 W/(m·K)] of the polybutylene terephthalate (PBT) packaging material. Thus, the case temperature does not have significant cyclic changes, and the thermal switch located outside of the device package is not able to perceive the device cyclic temperatures. However, converter loading and SiC heat losses change at time scales approaching 1–10 s for heavy-duty off road or train applications or solar panels, under which circumstances the thermal penetration depth is ~1 mm. The case temperature has distinct cyclic changes, and the thermal switch is able to respond to thermal cycling and reduce temperature swing of SiC devices. Moreover, the thermal time constant of the SiC device is ~1 s calculated by $\tau = R \cdot C$, where R is the thermal resistance and C is the thermal capacitance of the device.

To investigate the temperature swing reduction achieved by our thermal switch, we conducted transient simulations assuming the power converter loading changed with a period of 2 s between 0 and 5 kW and between 3 and 5 kW. Fig. 8 shows the simulation results for cyclic junction temperatures of hot SiC1 and cold SiC2 devices when integrated with an all-aluminum heat sink (Al ref) and the thermal switch (Switch) at a position of $x = 27$ mm. Fig. 8(a) shows that the heat losses change between 0 and 11.5 W for SiC1 and between 0 and 4.1 W for SiC2 when the converter power changes between 0 and 5 kW at a frequency of 0.5 Hz. The junction temperature of SiC1 swung between 40.9 °C and 42.5 °C for the Al heat sink indicated by the solid red line and between 46.3 °C and 47.7 °C for the thermal switch indicated by the dotted red line. For the cold SiC2 device, the junction temperatures' swing was between 36.9 °C and 37.5 °C for Al heat sink indicated by the blue solid line and 47.3 °C and 47.9 °C for thermal switch indicated by the blue dotted line. Fig. 8(b) shows that the heat losses change between 6.8 and 11.5 W for SiC1 and

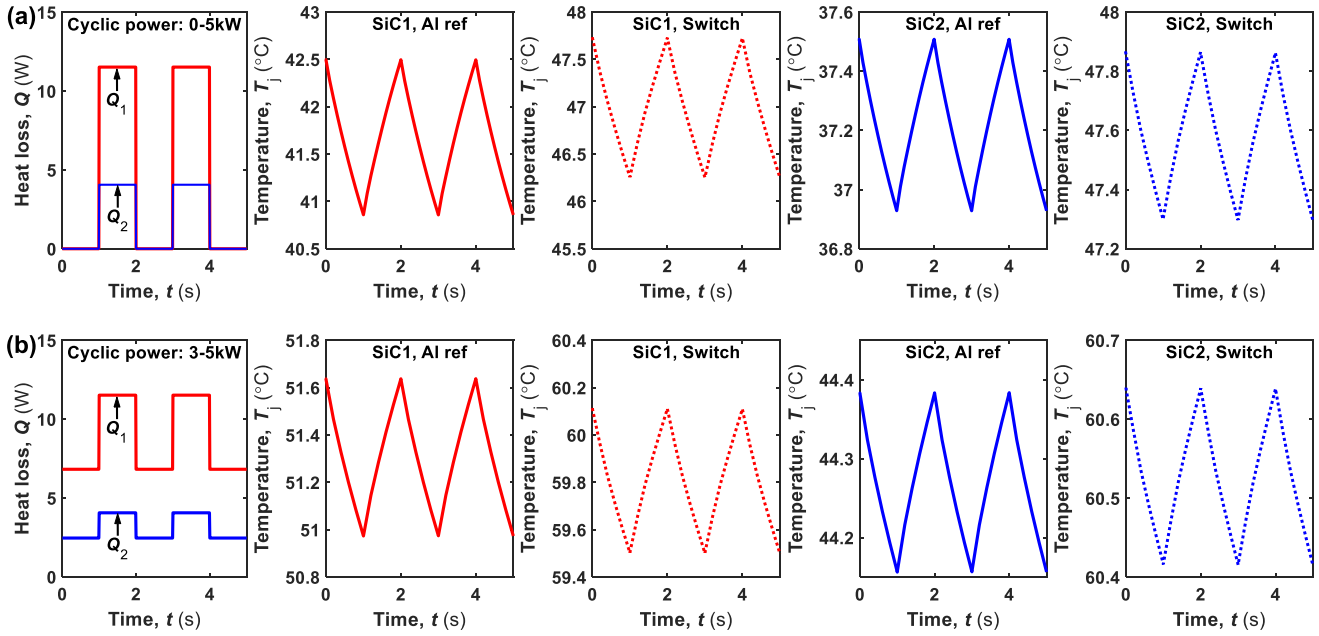

Fig. 8. Heat loss and junction temperature profiles of SiC1 and SiC2 integrated with an all-aluminum heat sink (Al ref) and the thermal switch (Switch) at a position of $x = 27$ mm when the power converter works at cyclic powers between (a) 0 and 5 kW and (b) 3 and 5 kW.

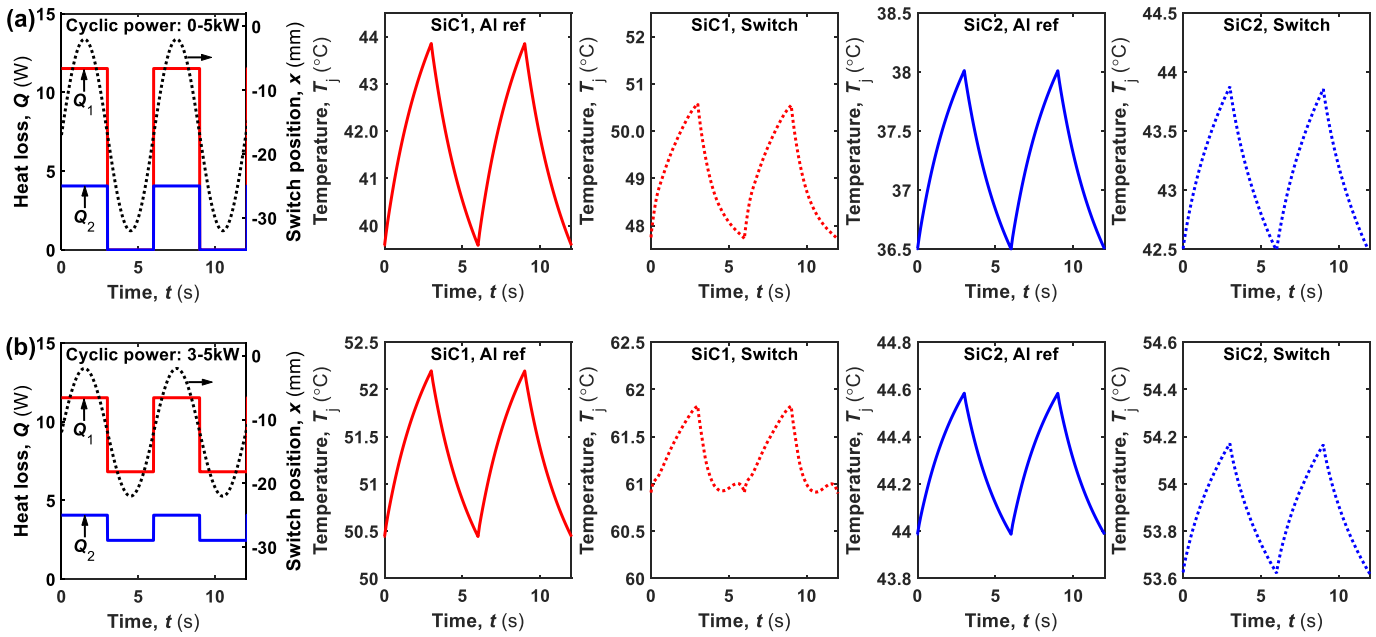

Fig. 9. Heat loss, thermal switch movement, and junction temperature profiles of SiC1 and SiC2 integrated with the Al ref and the switch when the switch moves periodically with the power converter working at cyclic powers between (a) 0 and 5 kW and (b) 3 and 5 kW.

between 2.5 and 4.1 W for SiC2 when the converter operates transiently between 3 and 5 kW. The junction temperature swing of hot SiC1 is 0.7 °C for Al heat sink and 0.6 °C for the thermal switch. The junction temperature swing of cold SiC2 is 0.2 °C for Al heat sink or the thermal switch. The junction temperature results show that our thermal switch reduces the temperature swings by 10% for hot SiC1 and 2% for cold SiC2 in the period of 2 s while maintaining isothermalization between SiC1 and SiC2 generally over a long timescale.

The thermal switch can be operated dynamically to further reduce the temperature swings of SiC devices. We conducted dynamic simulations assuming the thermal switch moves back and forth in the spreader channel according to the power converter operation in a period of 6 s. Fig. 9 shows the simulation results for cyclic junction temperatures of hot SiC1 and cold SiC2 devices when integrated with Al reference and dynamic switch. Fig. 9(a) shows the results for the power converter which operates between 0 and 5 kW in a period of 6 s where the thermal switch moves cyclically from

TABLE I
SUMMARY OF JUNCTION TEMPERATURE SWINGS, MAXIMUM TEMPERATURES, AND CYCLES TO FAILURE

Case	SiC device	ΔT_j (°C)		T_{max} (°C)		N_c		
		Al ref	Switch	Al ref	Switch	Al ref	Switch	Increase
A	SiC1	1.63	1.48	42.49	47.73	$2.8\text{x}10^{24}$	$4.6\text{x}10^{24}$	1.6X
(Fig. 8a)	SiC2	0.58	0.58	37.51	47.86	$15.2\text{x}10^{28}$	$8.1\text{x}10^{28}$	0.5X
B	SiC1	0.67	0.67	51.64	60.11	$9.4\text{x}10^{27}$	$11.6\text{x}10^{27}$	1.2X
(Fig. 8b)	SiC2	0.22	0.22	44.38	60.64	$14.1\text{x}10^{32}$	$3.3\text{x}10^{32}$	0.2X
C	SiC1	4.27	2.83	43.85	50.55	$1.6\text{x}10^{20}$	$53.1\text{x}10^{20}$	33.2X
(Fig. 9a)	SiC2	1.51	1.38	38.01	43.86	$9.4\text{x}10^{24}$	$13.2\text{x}10^{24}$	1.4X
D	SiC1	1.76	0.91	52.20	61.82	$5.3\text{x}10^{23}$	$1.8\text{x}10^{26}$	331.1X
(Fig. 9b)	SiC2	0.59	0.55	44.58	54.17	$6.5\text{x}10^{28}$	$5.5\text{x}10^{28}$	0.85X

$x = -2$ mm to $x = -32$ mm. The temperature swing for SiC1 was reduced by the dynamic switch to 2.8 °C from 4.3 °C of the Al reference design. The temperature swing for SiC2 was reduced by the dynamic switch to 1.4 °C from 1.5 °C of the Al reference design. Fig. 9(b) shows the results for the power converter which operates between 3 and 5 kW in a period of 6 s where the thermal switch moves cyclically from $x = -2$ mm to $x = -22$ mm. The temperature swing for SiC1 was reduced by the dynamic switch to 0.9 °C from 1.8 °C of the Al reference design. The temperature swing for SiC2 was reduced by the dynamic switch to 0.5 °C from 0.6 °C of the Al reference design. The simulation results show that the thermal switch reduces the temperature swings by 30%–50% for hot SiC1 and 6%–9% for cold SiC2, when moving dynamically according to the cyclic power of the converter. Simulations with different power converter operation periods show that the thermal switch can reduce temperature swings when the operation period is longer than 1 s and the thermal penetration depth is large enough so that the thermal switch can perceive the temperature change and achieve the desired temperature control. At longer operation periods, the thermal penetration depth is larger and the switch controllability to reduce temperature swings is better.

To quantify the improvement of SiC reliability due to temperature swing (ΔT_j) reduction enabled by our thermal switch, we calculated the device thermal lifetime quantified by the cycles to failure (N_c) based on the Coffin–Manson model. The model is defined as $N_c = A_1 \cdot (\Delta T_j)^{\alpha} \cdot \exp(A_2/T_m)$ [47], where $A_1 = 3.71 \times 10^{13}$, $\alpha = -10.122$, $A_2 = 9445.52$, and $T_m = T_{max} - \Delta T_j/2$. The Coffin–Manson model evaluates the benefit from reducing temperature swings ΔT_j and the penalty from ensuring higher device temperature T_m. The model was built to evaluate the thermo-mechanical effect on device reliability assuming no other mechanical or electrical damage exists or occurs during cycling. The lifetime calculation presents a qualitative comparison between our thermal switch and Al heat sink as the lifetime would decrease significantly if the power converter was operated at higher currents where devices would have higher temperatures. The model analyzed the device reliability in the presence of thermal switch or Al heat sink and did not investigate the reliability physics of the switch itself. Table I shows junction temperature swing ΔT_j, maximum junction temperature T_{max}, and the calculated thermal lifetime cycle N_c of SiC1 and SiC2 devices based on the simulation cases shown in Figs. 8 and 9. For the hot SiC1 device, the static thermal switch located at $x = 27$ mm increases the thermal lifetime by 1.6× or 1.2× when compared with Al reference for the converter operating cyclically between 0 and 5 kW or between 3 and 5 kW, respectively. Dynamic thermal switch integration increases the thermal lifetime by 33.2× or 331.1× when compared with Al reference for the converter operating cyclically between 0 and 5 kW or between 3 and 5 kW, respectively. For the cold SiC2 device, the thermal lifetime to failure is 2–5 orders of magnitude higher than hot SiC1, even though the thermal switch reduces the thermal lifetime to failure when compared with Al reference design. Overall, at the system level where hot SiC1 tends to fail earlier, our thermal switch improves the system reliability by enhancing hot SiC1 thermal lifetime to failure.

III. EXPERIMENT AND THERMAL MEASUREMENTS

Fig. 10 shows the thermal switch before and after integration with a single phase of the power converter along with a schematic of the experimental setup. The Cu thermal switch was embedded in the SS heat spreader and could move along the channel with a distance of x shown in Fig. 10(a). A thin layer (≈300 μm) of commercial lubricant (93 744, Super

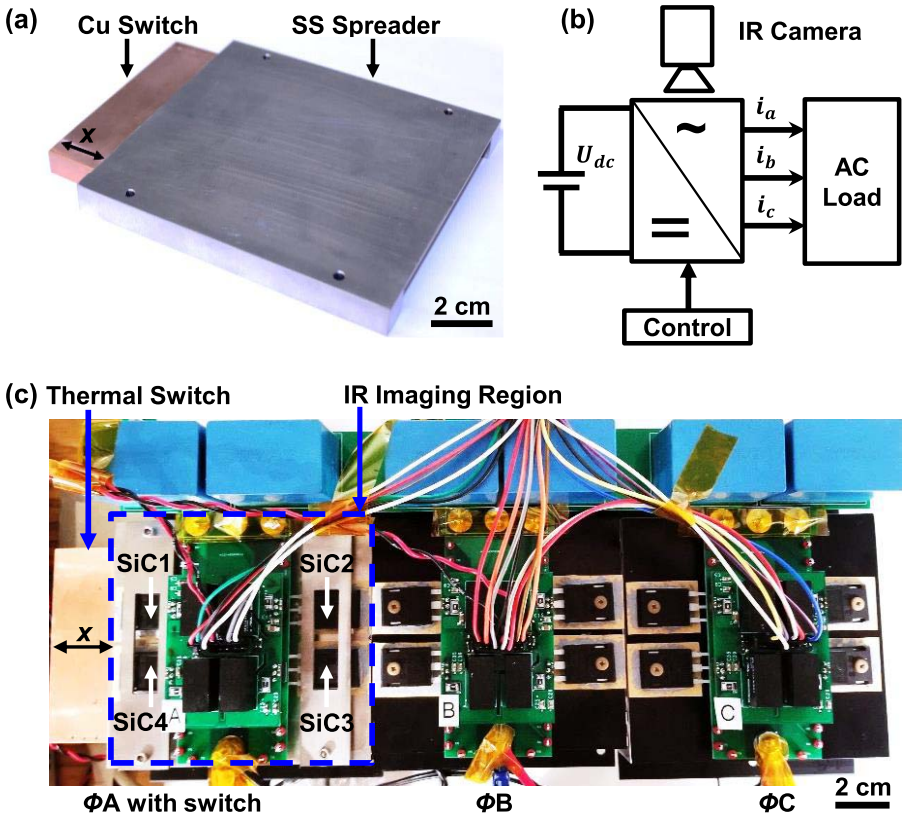

Fig. 10. (a) Isometric view of the manufactured heat spreader thermal switch showing the Cu switch at the $x = 20$ mm position. (b) Schematic of the experimental test rig used to characterize the performance of the thermal switch integrated with the prototype three-phase T-type converter. (c) Top-view photograph of the integrated thermal switch with the three-phase T-type converter. Phase A (ΦA) was integrated with the thermal switch and a conventional Al heat sink beneath it (not shown). Phase B (ΦB) and phase C (ΦC) were not integrated with the thermal switch and were instead cooled by conventional Al heat sinks (394-2AB, Wakefield-Vette).

Lube) was applied to the interface of the thermal switch and the heat spreader to facilitate easy sliding movement. Due to good wettability, we did not observe lubricant pump out of the interface during cyclic movement of the thermal switch in our experiments. Nevertheless, for real applications requiring long-time field operation, a risk of lubricant pump out exists, in which case lubricant resupply needs consideration. Thermal interface materials were attempted to be used as a replacement of the lubricant, with limited efficacy due to the lack of lubricity (high viscosity) needed to enable smooth motion of Cu switch. The low thermal conductivity [$\approx$ 0.6 W/(m·K)] of the lubricant resulted in a large interfacial thermal resistance and increased isothermal temperatures, which will be discussed later in finite volume method (FVM) simulations. Fig. 10(b) shows a schematic of the experimental setup. The power converter converted a dc voltage from a dc power supply (XR 375-26.5/380+HS+LXI, Magna-Power Electronics) into three-phase ac voltage applied to an ac load consisting of capacitors, inductors, and resistors. Three-level space-vector modulation (SVM) controlled the converter to generate 60-Hz output voltages with 20-kHz switching frequency. The SVM control scheme was implemented with a digital signal processing (DSP) unit (Texas Instruments, TMS320F28335). An infrared (IR) camera (A655sc, FLIR) was used to obtain the temperature profile of phase A (ΦA) integrated with our thermal switch as shown in Fig. 10(c). The integrated thermal switch and the other two phases without thermal switches (ΦB and ΦC) were each cooled by single and independent Al heat sinks (394-2AB, Wakefield-Vette). Airflow at a volumetric flow rate of 35.9 CFM at the room temperature was delivered by independent fans (8500DP, ebm-papst Inc.) rotating at 3200 RPM beneath each heat sink (not shown in Fig. 10). The fan speed was chosen based on the rated speed which resulted in turbulent flow between the fins. Prior to running experiments, a hot wire anemometer was used to measure the fan speed between each phase at the center of the fan, showing a deviation of $<2\%$ from phase-to-phase. Mounting of thermal management was achieved using a commercial gap pad (SIL-PAD 400, BERGQUIST) having a thermal conductivity of 0.9 W/(m·K) and a thickness of $\approx$200 μm. Hot SiC devices in ΦB spread a certain amount of heat to adjacent cold SiC devices (SiC2 and SiC3) in ΦA, which reduced the measured hot-to-cold device temperature difference (ΔT) in our experiments. The blue dashed box [see Fig. 10(c)] indicates the IR imaging region, which focused on four SiC devices (SiC1, SiC2, SiC3, and SiC4). The heat spreader thermal switch was integrated with ΦA and the conventional Al heat sink using four socket screws, which were assembled using a torque of 0.042 N·m with a torque screwdriver (S0-24, Seekonk) for SiC device safety and consistency of compression force.

After the thermal switch was moved to a certain position x and the system reached thermal steady state, thermal images were recorded for analysis. Prior to imaging, the IR camera was calibrated to ensure accurate device emissivity using a small piece of highly emissive black tape adhered directly on SiC device. After adhering the black tape, the converter was turned on gradually with SiC device temperature ranging from 25 °C to 70 °C in 5 °C increments, enabling accurate characterization of temperature-dependent SiC case emissivity. The detectable temperature difference of the IR camera is as small as 50 mK, good enough to provide a consistent temperature comparison between hot and cold SiC devices. It is necessary to point out that we only demonstrated thermal switch integration with ΦA since the other two phases have a similar circuit layout and heat loss profile. The hot SiC devices on the left side of ΦB spread heat to adjacent phase A and warm up cold SiC devices (SiC2 and SiC3) shown in Fig. 10(c). The heat transfer pathway from ΦB will be addressed later using 3-D FVM simulations of ΦA by tuning the junction-to-bottom thermal impedances of SiC2 and SiC3.

Fig. 11 shows the zoomed-in ΦA thermal images when Cu thermal switch was moved to different positions. For these experiments, the power converter operated at 2.4 kW with the Al heat sink beneath the thermal switch cooled by air forced convection. The power level was limited below 3 kW because the SiC devices used in our experiments have an alternating current rating of 19 A that decreases to 10 A when the device temperature increases to 120 °C. The case temperatures of hot SiC1 and SiC4 devices decreased slightly as x increased due to more efficient heat spreading through thermal switch. On the contrary, the case temperatures of cold SiC2 and SiC3 increased with increasing x due to less efficient heat transfer through the SS air channel after the Cu thermal switch moved further away from the devices. The hot and cold SiC devices had the same case temperature of 41.5 °C when the thermal switch moved to $x = 20$ mm. The hot area in the center of each thermal image consisted of ΦA gate drivers, which consisted of the common-mode filter, isolated power supply, logic circuitry, and driver circuitry. The gate drivers had a constant temperature profile and were not affected by Cu thermal switch movement due to the gate driver being suspended on top of the phase leg circuit PCB, eliminating physical contact with the thermal switch. From the thermal images, T_{Hot} was obtained by averaging the maximum temperatures of SiC1 and SiC4 devices and T_{Cold} was obtained by averaging the maximum temperatures of SiC2 and SiC3 devices.

IV. Thermal Analysis by FVM Simulation

To verify the experimental results, model the thermal pathways of the prototype, and study the key parameters that dominate isothermalization capability of the heat spreader thermal switch, a separate 3-D FVM simulation was developed (see Fig. 12). Computational fluid dynamics (CFD) FVM simulations were used to model the heat and mass transfer, since the heat transfer coefficient distribution was highly nonuniform due to the nonuniform velocity of the air delivered by a fan perpendicularly to heat sink fins. The CFD FVM model consisted of ΦA of the power converter, the SS heat spreader, the Cu thermal switch, and the Al heat sink cooled by the airflow from a fan [see Fig. 12(a)]. To simulate forced convection, a cabinet containing the whole assembly and the air as the working fluid was built, but not shown for clarity. The cabinet had four side walls 110 mm away from the assembly, one bottom opening 110 mm away from the bottom heat sink, and one top opening 500 mm away from the top PCB. The airflow field delivered by the fan from the bottom opening was computed by solving the coupled Navier–Stokes equations, heat equation, and the characteristic equation of the fan volume flow rate versus pressure drop characteristics. Prior to running the simulations, meshing of the solid and air domains was done separately to reduce mesh complexity. The PCB-mounted SiC devices, the heat spreader thermal switch, and heat sink were meshed as separate parts to avoid mesh bleeding due to high aspect ratios of the PCB, SiC device leads, and gap pads. The mesh density of the PCB-mounted SiC devices was five times that of the heat spreader thermal switch and ten times the heat sink and air domain. Grid independence was checked by comparing the simulation results with finer meshes. After 100 iterations, the computation converged with residuals less than 1×10^{-4}. A turbulent solver using the two-equation turbulence model was applied with Reynolds number $\text{Re} > 50\,000$. The thermal properties of air such as density and thermal conductivity were modeled to be temperature-dependent. The remaining materials in the simulation domain were modeled assuming constant properties. A side view of the FVM model domain is shown in Fig. 12(b), labeling the key thermal contact resistances: $R_{\text{spreader}-\text{switch}}$ between the heat spreader and the thermal switch, and $R_{\text{switch}-\text{HS}}$ between the thermal switch and the heat sink. The thermal contact resistances dominated the thermal impedances from the heat spreader thermal switch and affected the heat transfer performance adversely. Heat transfer pathways from the SiC device junction were affected by the thermal resistances from the junction to the six surfaces of the package, as shown with a simplified thermal resistance diagram in Fig. 12(c). Real SiC devices were not easy to model due to the complicated internal SiC chip structure, wires to the three leads, metal spreader, and plastic package. For steady-state thermal modeling, the dominant parameters were the thermal resistances which were obtained from the SiC device manufacturer datasheet [48], eliminating the need to model the entire device structure using heat generation at the junction node. Therefore, only the SiC junction-to-side (R_{j-s}), junction-to-top (R_{j-t}), and junction-to-bottom (R_{j-b}) thermal resistances were modeled in our 3-D FVM simulations by referring to the SiC device datasheet and experimental results. In the real experiments, heat transfer in ΦA of the power converter was affected by adjacent ΦB hot SiC devices shown in Fig. 10(c), which acted to increase the temperatures of cold SiC devices in ΦA. Our FVM model focused on the thermal switch integrated ΦA to save computational time and cost. To simulate the heat transfer pathways from adjacent ΦB, the thermal resistance R_{j-b} of cold SiC devices neighboring hot SiC devices in ΦB was iterated by fitting with the experimental results. Heat losses calculated from a precise circuit loss model were applied to the junction nodes of SiC devices, modeled as heat sources.

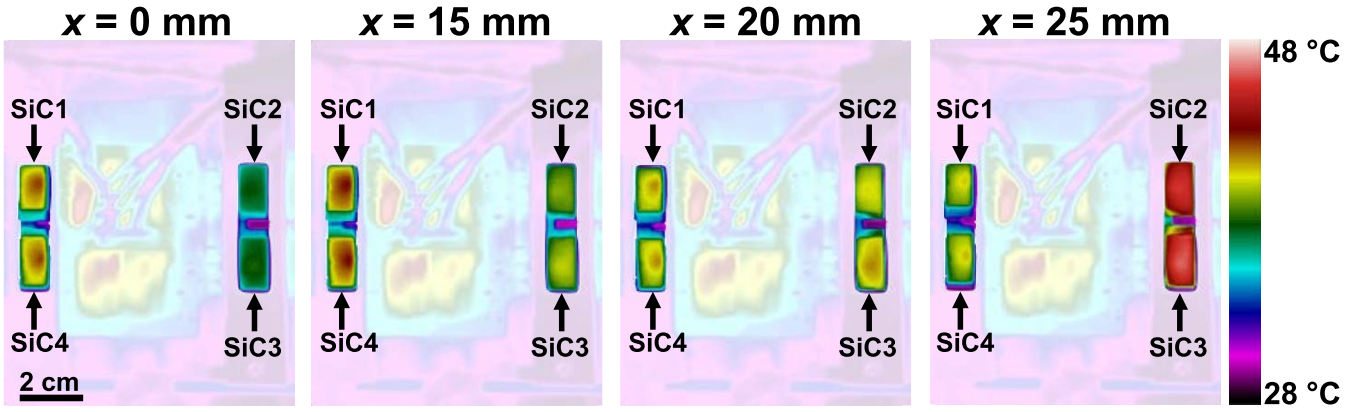

Fig. 11. Top-view IR images of ΦA [see Fig. 9(c)] with the Cu thermal switch at different positions (x). The converter was operated at a power input of 2.4 kW, while the Al heat sink beneath the thermal switch was cooled by forced convection of airflow using a fan. The background is blurred to show the SiC devices more clearly.

With thermal resistances and heat losses as input parameters, the temperature distribution and air velocity field were solved with FVM simulation. A combination of FVM simulations and experimental results determined the key parameters to analyze the thermal performance of the thermal switch to isothermalize SiC devices.

Table II summarizes the heat losses and thermal resistances when the power converter operated at different conditions. In case i, the power converter was operated with an input power of 2.4 kW. The heat losses Q_1 from each hot SiC device and Q_2 from each cold SiC device were analyzed by a real-time loss model with converter power, switching frequency, and temperatures as input parameters [38]. In case ii, the input power of the converter decreased to 2.2 kW, which lowered heat losses Q_1 and Q_2. In case iii, the fan was turned off and the heat sink was cooled by air natural convection, while the power converter operated at 2.2 kW. Comparing case iii with case ii having the same converter power, the temperature-dependent heat losses increased owing to higher conduction losses of the less efficient SiC devices [38], since the temperatures of SiC devices increased due to less efficient heat removal from natural convection (case iii). The thermal contact resistances $R_{\text{spreader}-\text{switch}}$ and $R_{\text{switch}-\text{HS}}$ were estimated from previous work [41] and determined by fitting our 3-D FVM results with our experimental results. The thermal resistances of SiC device were obtained from the manufacturer datasheet [48]. However, the junction-to-bottom thermal resistance $R_{j-b,\text{cold}}$ of cold SiC devices was variable to account for the heat transfer pathway from adjacent hot SiC devices of ΦB, which warmed up the cold SiC devices of ΦA. The effect of the added heat transfer pathway was facilitated by more lateral heat spreading and less heat sink cooling due to natural convection, resulting in larger $R_{j-b,\text{cold}}$ in case iii when compared with cases i and ii.

The FVM simulation results of case i are shown in Fig. 13, using key parameters from Table II in the model. The hot SiC1 and SiC4 devices had average case temperatures of 42 °C, approximately equivalent to SiC2 and SiC3 devices when the thermal switch was moved to $x = 20$ mm [see Fig. 13(a)]. The heat loss from SiC devices was transferred mostly from the heat spreader thermal switch to the heat sink, partially through Cu electrical connections to the PCB, and partially from the package to the surrounding ambient air at 25 °C via natural convection. Fig. 13(b) shows the temperature profile of cross section A-A depicted in Fig. 13(a). The thermal switch conducted heat more efficiently from hot SiC devices; however, the air channel embedded in the SS heat spreader conducted heat less efficiently from cold SiC devices, resulting in a larger temperature gradient in the channel under SiC2 [see Fig. 13(b)]. The Al heat sink beneath the thermal switch transferred the heat convectively to the airflow indicated by the black arrows. The movement of the thermal switch caused asymmetric airflow around ΦA of the converter. The precise FVM models developed here matched the experimental results well, enabling us to predict thermal performance of the thermal switch and design thermal switches for different electronics designs.

V. Results and Discussion

Fig. 14 shows the experimental and simulation temperature results of hot and cold SiC devices as a function of thermal switch position for cases i, ii, and iii (see Table II). The excellent agreement between the simulations and experiments indicated that the developed FVM simulation was successful at predicting the thermal switch performance and hence was used to analyze key thermal resistances in the integrated assembly. For case i depicted in Fig. 14(a) and case ii in Fig. 14(b), hot SiC device temperatures decreased slightly with increasing switch position. However, cold SiC device temperatures increased slowly for $x < 15$ mm, rapidly for 15 mm $< x <$ 40 mm, and slowly again for $x > 40$ mm, which indicated that the switching effect was most obvious when the thermal switch was moved in close proximity to cold SiC devices. When the thermal switch moved to $x = 20$ mm, hot SiC devices had the same temperature as cold SiC devices. The similar temperature trend of hot and cold SiC devices was demonstrated for case iii [see Fig. 14(c)]. However, the isothermalization position of thermal switch was reduced to $x = 17$ mm due to less efficient heat transfer from natural convection. The experimental and simulation results demonstrated that the solid heat spreader

TABLE II
LIST OF HEAT LOSSES AND THERMAL RESISTANCES

Case	Power, P (kW)	Cooling Method	Q_1 (W)	Q_2 (W)	$R_{\text{spreader-switch}}$ ((mm^2·K)/W)	$R_{\text{switch-HS}}$ ((mm^2·K)/W)	$R_{\text{j-t}}$ (K/W)	$R_{\text{j-s}}$ (K/W)	$R_{\text{j-b, hot}}$ (K/W)	$R_{\text{j-b, cold}}$ (K/W)
i	2.4	Air Forced Convection	4.7	1.7						1.2
ii	2.2	Air Forced Convection	4.1	1.5	500	500	6	12	0.4	1.2
iii	2.2	Air Natural Convection	4.3	1.6						2.0

thermal switch is capable of achieving isothermalization of SiC devices by moving the switch to different positions tailored for this particular power converter operating at different working conditions.

For future real-world applications such as SiC traction drive systems, much higher powers must be considered. To explore the feasibility of our thermal switch to isothermalize SiC devices dissipating higher heat loads, we used our 3-D FVM model to predict the heat spreader thermal switch performance when the power converter operates at higher powers. Fig. 15 shows the predicted temperature results of hot and cold SiC devices as a function of switch position when the power converter operates at 3.5 and 5.0 kW. The hot SiC device dissipated a heat loss of 9.3 W, while the cold SiC device dissipated 3.3 W when the power converter operated at 3.5 kW. When the operation power was increased to 5.0 kW, the hot SiC device dissipated 14.5 W and the cold SiC device dissipated 5.1 W. Forced convection of ambient air was applied to cool down the system. The power level of 5.0 kW is the maximum input power our converter can process theoretically, considering the SiC current derating as a function of temperature. Similar trends of hot and cold SiC device temperatures are shown in Fig. 15(a) for 3.5 kW and Fig. 15(b) for 5.0 kW compared with 2.4 kW in Fig. 14(a). However, thermal switch isothermalization position moves slightly further away from cold SiC devices with 20 mm for 2.4 kW, 21 mm for 3.5 kW, and 21.5 mm for 5.0 kW. The predications indicate that our thermal switch can control temperatures and achieve isothermalization of SiC devices operating at high powers.

The successful demonstration studied here shows the feasibility of using a thermal switch to reduce the temperature difference between SiC devices when compared with the conventional fixed thermal management methods. The thermal switch can be used as a tool in converter designs to tune individual component temperatures and achieve greater temperature uniformity as an active thermal management method. For example, converter components have optimal operating temperatures governed by set objectives such as reliability and power density [44], [45]. The thermal switch can be an efficient tool to maintain components working at optimal temperature ranges. For nonplanar converters designed by 3-D packaging principles [12], overall thermal integration with a thermal switch is able to reduce highly localized temperatures by sharing heat among components and achieve meaningful improvements in temperature uniformity while maintaining high power density. In addition, low-cost SS material, comprehensive design, and straightforward manufacture and integration make the thermal switch applicable to multiple electronics platforms other than wide bandgap power semiconductor power converters. The relatively easy scale up indicates that the thermal switch can be customized for both low- and high-power applications. The integrated thermal switch design demonstrated here is flexible for other shapes or materials when compared with thermoelectric switches or VCHP switches.

To actuate the thermal switch for isothermalization of power converters operating in transient applications, actuation approaches need to be considered. A plethora of power dense actuation systems exist, such as electrical, pneumatic, hydraulic, magnetic, or electro-mechanical [49]–[56]. Selection and integration is a key design parameter. For the application scenarios studied in this work, the power converter operated at a static power with a constant power factor during long time durations. Thus, the thermal switch was kept in a static position to achieve device-to-device isothermalization. However, when the converter works in a transient fashion, thermal switch motion is necessary for isothermalization. While dynamic thermal switch operation helps reduce device temperature swings, static thermal switch operation reduces device-to-device temperature difference at the isothermal position. Future research could explore the combination of the two options of dynamic thermal switching and static thermal switching, considering power converter layout and operation conditions, switch position, geometry optimization, and materials' selection.

To respond to changing power levels of the converter, the actuator and the control system must be designed accordingly to keep both precise actuation distance and speed.

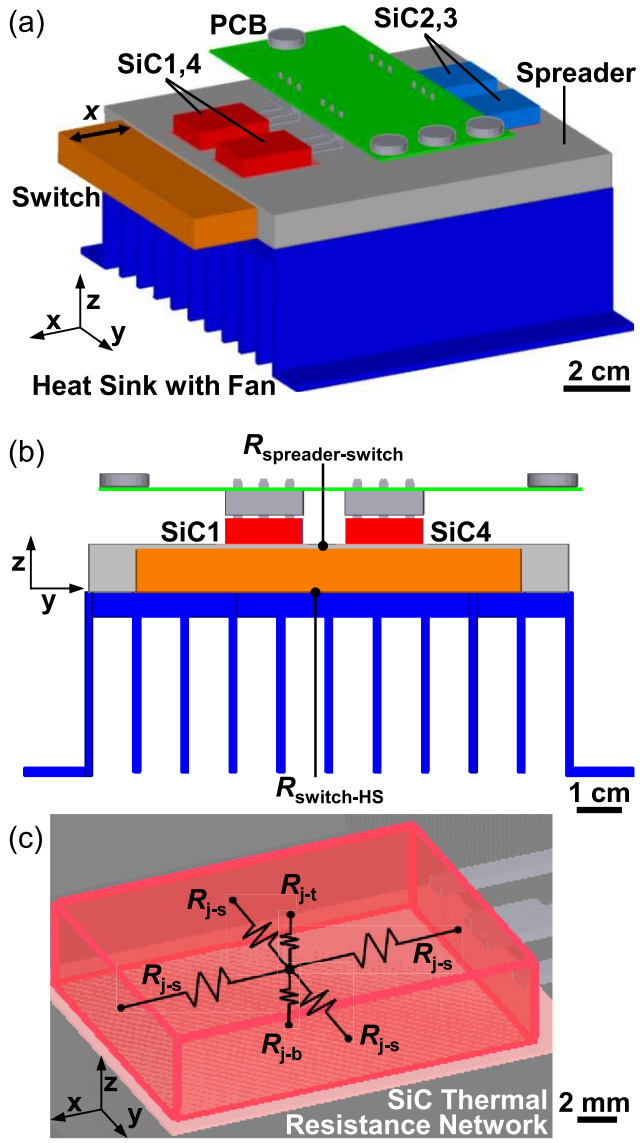

Fig. 12. (a) Three-dimensional FVM simulation model built to analyze the heat transfer of ΦA of the power converter integrated with the thermal switch, including the external air-side heat dissipation mechanism. The fan, having a known volumetric flow rate versus pressure drop relation (8500DP, ebm-papst Inc.), is not shown for clarity. (b) Side view of the FVM model depicted in (a) showing the key thermal contact resistances between the heat spreader and the thermal switch ($R_{\text{spreader}-\text{switch}}$) and the thermal switch and the heat sink ($R_{\text{switch}-\text{HS}}$). (c) Simplified thermal resistance network of a single SiC device showing the effective thermal resistances from the junction to the six surfaces of the device package. Relevant thermal resistances were obtained from the manufacturer datasheet [48].

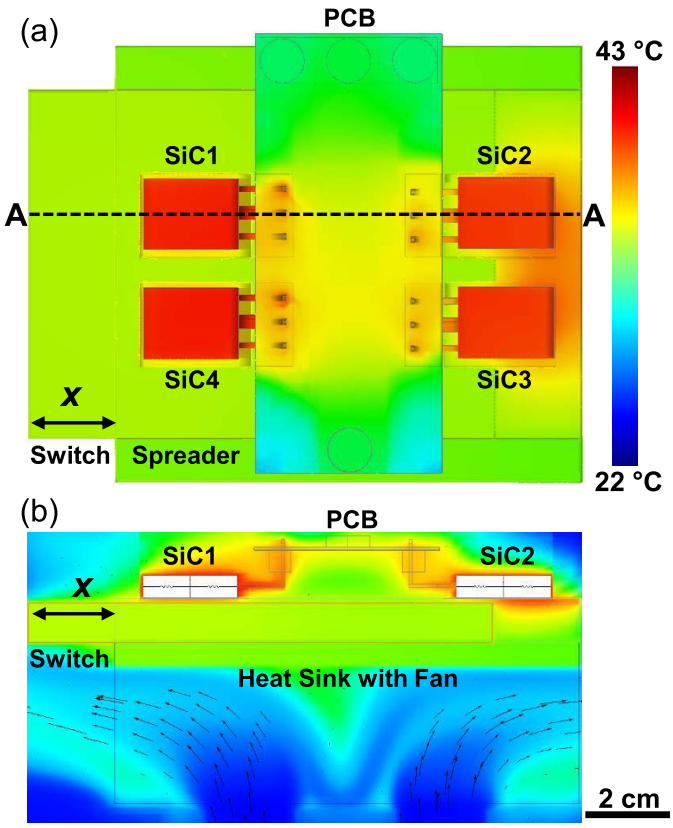

Fig. 13. (a) Top-view FVM simulation temperature distribution of ΦA with thermal switch at $x = 20$ mm to isothermalize SiC devices. The simulated converter operated at 2.4 kW with the heat sink cooled by forced convection. (b) Front view of cross section A-A, showing the converter and air temperature distributions. Black arrows represent the airflow velocity, with the maximum arrow size representing 6 m/s. Flow asymmetry arose due to the asymmetric shape of the thermal switch, which blocked airflow on the left side. Heat transfer coefficient was not applied as the boundary condition, while the thermal transport within the fluid domain was resolved in CFD numerical simulation, which evaluated an average heat transfer coefficient $\approx$ 100 W/(m^2·K) in terms of the base area of heat sink.

The response speed is important for thermal switch reliability. High speed and temperature should be considered due to the impact on the thermal switch gaps filled with lubricant oil, although the impact was negligible at low speeds and temperatures used in our experiments. In addition, optimized control algorithms for switch motion need to be developed for the maximum reduction in temperature swing or gradient. Feed-forward control is a potential approach. The main challenges include thermal switch inertia, which limits the response speed, and frequency of device power oscillation which limits the thermal penetration depth at high frequency. Due to the intrinsic heterogenous temperature distribution inside SiC devices, the temperature gradients and swings cannot be eliminated completely but can be reduced to an acceptable range using optimized control strategies and thermal switch design. Overall, the codesign of the actuation system with the converter system is required to minimize volume and mass, while maximizing power density and reliability for future thermal switch applications. Despite the significant number of advantages, the thermal switch has some disadvantages such as additional weight to the electronic system and added junction-to-coolant thermal impedance. The resulting gravimetric power density reduction and heat load increase must be considered as the main tradeoff with lower thermal stresses and greater reliability when designing future electronic systems.

Both the simulations and experiments showed that the thermal switch was most effective at manipulating heat transfer when moving close to heat dissipating SiC devices. Future designs should focus on changing the thermal conductances near the heat sources. Further work is needed on power

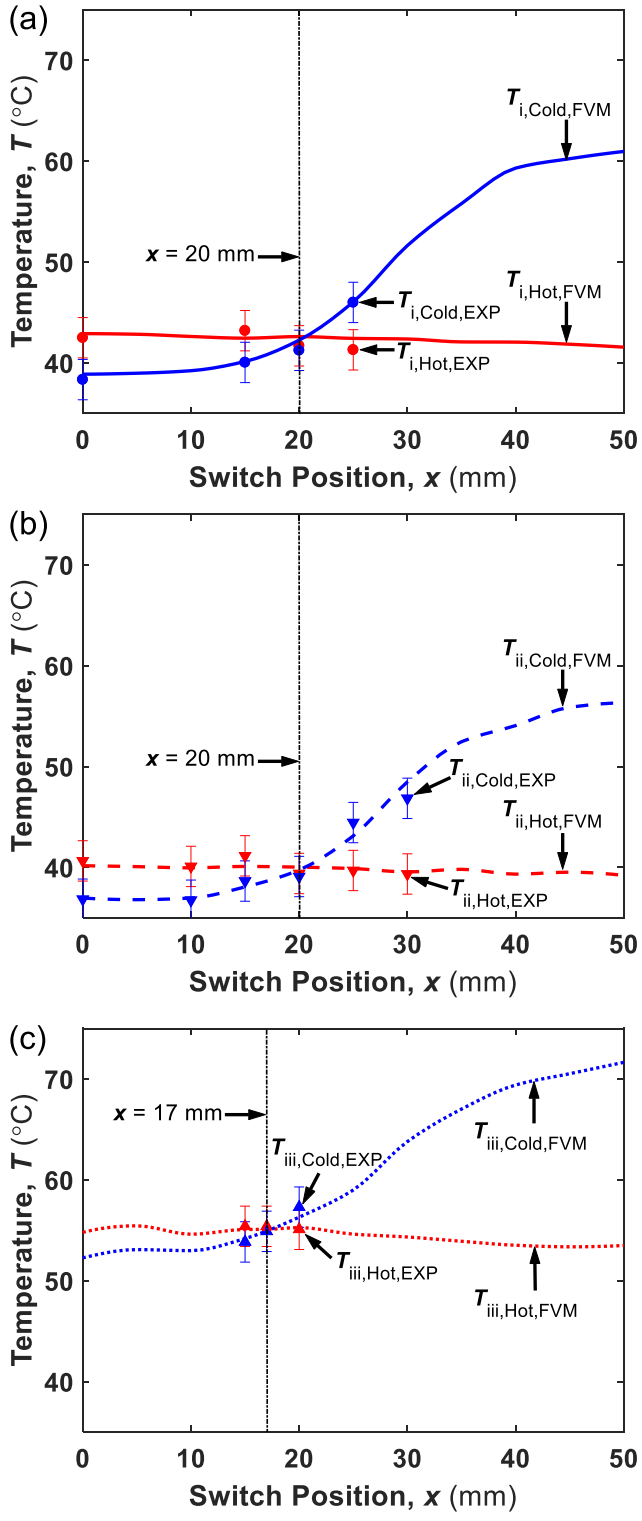

Fig. 14. Hot SiC device (SiC1, SiC4) and cold SiC device (SiC2, SiC3) temperatures as a function of Cu switch position (x) for (a) Table II, case i; (b) Table II, case ii; and (c) Table II, case iii. The lines represent predictions obtained from FVM simulations. The data points represent experimental results. The error in experiment temperature measurement was ±2.0 °C stemming from the calibrated IR thermal measurement.

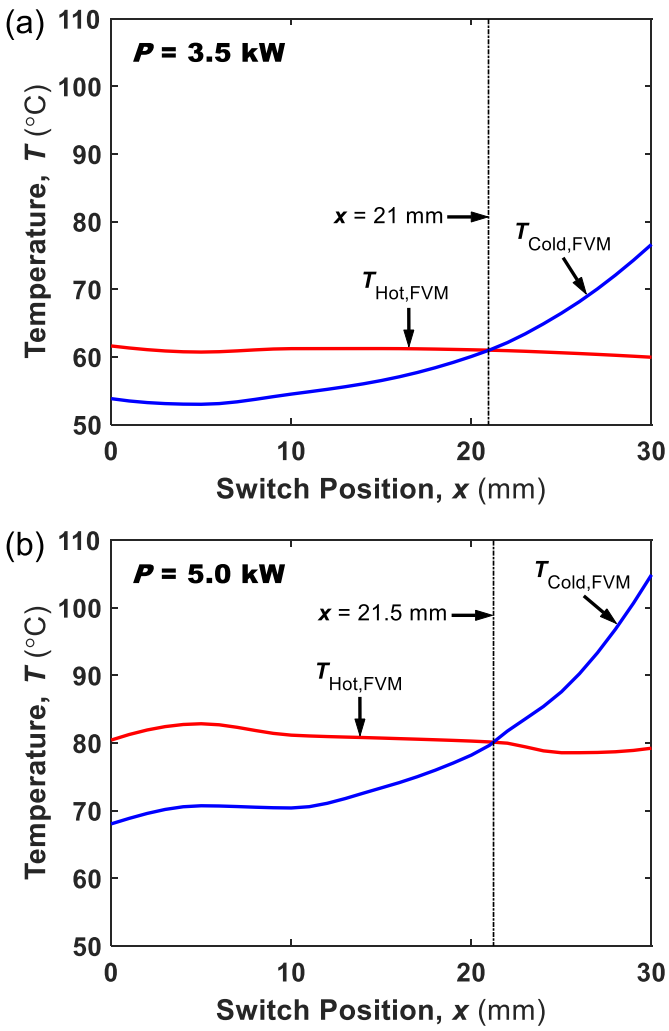

Fig. 15. Hot SiC device (SiC1, SiC4) and cold SiC device (SiC2, SiC3) temperatures as a function of Cu switch position (x) for converter powers of (a) 3.5 kW and (b) 5.0 kW, obtained from FVM predictions. The power converter system was cooled by forced convection with air to a back-side Al heat sink.

density enhancement by reducing the thermal switch mass by removing extra material further away from heat sources. Thus, specific power density can be enhanced, and energy cost for thermal switch actuation can be reduced. In addition to the steady thermal switch operation shown here, the active heat spreader thermal switch is able to enable isothermalization of SiC devices continuously by moving the thermal switch even if the power converter works in transient conditions. For example, the movement of the thermal switch can be programmed to be periodic when the power converter works under a cyclic loading condition. Active feedback control can be used to modulate the thermal switch position for highly transient and nonperiodic drive cycles. Such real-time heat transfer control is currently not possible with nonhomogeneous heat exchangers or modular heat sinks with fixed structures. Furthermore, high-frequency movement of the thermal switch for transient applications may lead to degradation and pump out of the thermal interface material. Future work on the reliability of the thermal switch is required to ameliorate these concerns. In addition, using FEM and FVM simulations developed here, the heat spreader thermal switch can be customized and evaluated for other power electronics applications. Finally, the thermal

switch can also be combined with other thermal management methods such as phase change materials to stabilize electronics temperature temporally and enable overall downsizing of the entire thermal management system [57], [58]. Considering different thermal management methods, the cooling boundary conditions differ for various designs of the thermal switch requiring different geometries and materials to be optimized. For example, using a high-performance microchannel cold plate can transfer the majority of heat losses more efficiently through the switch when compared with forced or natural air convection heat sinks. Thus, heat flow and temperature controllability of our thermal switch can be enhanced and a downsized thermal switch can be realized to enhance the overall power density.

VI. Conclusion

We studied the isothermalization performance of a solid heat spreader thermal switch to reduce the temperature differences between hot and cold SiC devices of a three-level T-type power converter. The spreader switch consists of a Cu thermal switch embedded in an SS heat spreader. When the converter was operated at 2.4 kW, each hot SiC device dissipated 4.7 W at a steady case temperature of 43 °C, while each cold SiC device dissipated 1.7 W at a case temperature of 38 °C. The thermal switch reduced the temperature difference from 5 °C to 0 °C by improving junction-to-coolant heat transfer from hot SiC devices and reducing heat transfer from cold SiC devices when the switch was moved to the position of 20 mm. When the converter operated at 2.2 kW, the temperature difference was reduced to 0 °C by moving the thermal switch to 20 mm, and with the heat sink cooled by natural convection, a switch position of 17 mm resulted in isothermalization. Detailed 3-D FEM and FVM simulations were developed to investigate the heat transfer mechanisms of the integrated thermal switch. The simulation results were validated by single-phase prototype experiments and were used to analyze key parameters dominating isothermalization performance of the thermal switch. The validated FVM simulations were used to predict thermal switch performance at higher converter powers and represent a good starting point for future electro-thermal codesign. This work demonstrates the capability of our thermal switch to isothermalize active components on a particular power converter design to achieve improved temperature uniformity.

References

[1] H. Wang, M. Liserre, and F. Blaabjerg, "Toward reliable power electronics: Challenges, design tools, and opportunities," *IEEE Ind. Electron. Mag.*, vol. 7, no. 2, pp. 17–26, Jun. 2013, doi: 10.1109/MIE.2013.2252958.

[2] D. Huitink, K. Enamul, S. Rangaraj, and A. Lucero, "Acceleration of chip—Package failures in temperature cycling," in *Proc. IEEE Int. Rel. Phys. Symp.*, Jun. 2014, pp. 1–4, doi: 10.1109/IRPS.2014.6860608.

[3] S. Yang, A. Bryant, P. Mawby, D. Xiang, L. Ran, and P. Tavner, "An industry-based survey of reliability in power electronic converters," *IEEE Trans. Ind. Appl.*, vol. 47, no. 3, pp. 1441–1451, May/Jun. 2011, doi: 10.1109/TIA.2011.2124436.

[4] K. Ma, M. Liserre, F. Blaabjerg, and T. Kerekes, "Thermal loading and lifetime estimation for power device considering mission profiles in wind power converter," *IEEE Trans. Power Electron.*, vol. 30, no. 2, pp. 590–602, Feb. 2015, doi: 10.1109/TPEL.2014.2312335.

[5] M. Ciappa, "Selected failure mechanisms of modern power modules," *Microelectron. Rel.* vol. 42, nos. 4–5, pp. 653–667, Apr. 2002, doi: 10.1016/S0026-2714(02)00042-2.

[6] T. Liu *et al.*, "Tunable, passive thermal regulation through liquid to vapor phase change," *Appl. Phys. Lett.*, vol. 115, no. 25, Dec. 2019, Art. no. 254102, doi: 10.1063/1.5133795.

[7] B. Kwon, T. Foulkes, T. Yang, N. Miljkovic, and W. P. King, "Air jet impingement cooling of electronic devices using additively manufactured nozzles," *IEEE Trans. Compon., Packag., Manuf. Technol.*, vol. 10, no. 2, pp. 220–229, Feb. 2020, doi: 10.1109/tcpmt.2019.2936852.

[8] E. Laloya, Ó. Lucía, H. Sarnago, and J. M. Burdío, "Heat management in power converters: From state of the art to future ultrahigh efficiency systems," *IEEE Trans. Power Electron.*, vol. 31, no. 11, pp. 7896–7908, Nov. 2016, doi: 10.1109/TPEL.2015.2513433.

[9] T. Yang *et al.*, "An integrated liquid metal thermal switch for active thermal management of electronics," *IEEE Trans. Compon., Packag., Manuf. Technol.*, vol. 9, no. 12, pp. 2341–2351, Dec. 2019, doi: 10.1109/tcpmt.2019.2930089.

[10] S. Jones, D. Pye, and P. Jeal, "Modern materials technologies in PCB thermal management," in *Proc. IEE Colloquium CAD Comput. Aided Des. Tools Thermal Manage.*, 2002, pp. 1–9.

[11] E. C. W. de Jong, J. A. Ferreira, and P. Bauer, "Thermal design based on surface temperature mapping," *IEEE Power Electron Lett.*, vol. 3, no. 4, pp. 125–129, Dec. 2005, doi: 10.1109/LPEL.2005.860625.

[12] E. C. W. de Jong, J. A. Ferreira, and P. Bauer, "Design techniques for thermal management in switch mode converters," *IEEE Trans. Ind. Appl.*, vol. 42, no. 6, pp. 1375–1386, Nov. 2006, doi: 10.1109/TIA.2006.882674.

[13] K. Desingu, R. Selvaraj, and T. R. Chelliah, "Control of reactive power for stabilized junction temperature in power electronic devices serving to a 250-MW asynchronous hydrogenerating unit," *IEEE Trans. Ind. Appl.*, vol. 55, no. 6, pp. 7854–7867, Nov. 2019, doi: 10.1109/TIA.2019.2933514.

[14] P. K. Prasobhu, G. Buticchi, S. Brueske, and M. Liserre, "Gate driver for the active thermal control of a DC/DC GaN-based converter," in *Proc. IEEE Energy Convers. Congr. Expo. (ECCE)*, Sep. 2016, pp. 2–9, doi: 10.1109/ECCE.2016.7855131.

[15] M. Andresen, K. Ma, G. Buticchi, J. Falck, F. Blaabjerg, and M. Liserre, "Junction temperature control for more reliable power electronics," *IEEE Trans. Power Electron.*, vol. 33, no. 1, pp. 765–776, Jan. 2018, doi: 10.1109/TPEL.2017.2665697.

[16] A. Masood *et al.*, "Comparison of heater architectures for thermal control of silicon photonic circuits," in *Proc. 10th Int. Conf. Group IV Photon.*, Aug. 2013, pp. 83–84, doi: 10.1109/Group4.2013.6644437.

[17] A. Ribeiro and W. Bogaerts, "Digitally controlled multiplexed silicon photonics phase shifter using heaters with integrated diodes," *Opt. Exp.*, vol. 25, no. 24, p. 29778, Nov. 2017, doi: 10.1364/oe.25.029778.

[18] M. Bahadori *et al.*, "Thermal rectification of integrated microheaters for microring resonators in silicon photonics platform," *J. Lightw. Technol.*, vol. 36, no. 3, pp. 773–788, Feb. 1, 2018, doi: 10.1109/JLT.2017.2781131.

[19] K. Padmaraju, D. F. Logan, X. Zhu, J. J. Ackert, A. P. Knights, and K. Bergman, "Integrated thermal stabilization of a microring modulator," *Opt. Exp.*, vol. 21, no. 12, pp. 14342–14350, Jun. 2013, doi: 10.1364/oe.21.014342.

[20] D. W. Hengeveld, M. M. Mathison, J. E. Braun, E. A. Groll, and A. D. Williams, "Review of modern spacecraft thermal control technologies," *HVAC R Res.*, vol. 16, no. 2, pp. 189–220, Feb. 2010, doi: 10.1080/10789669.2010.10390900.

[21] G. Wehmeyer, T. Yabuki, C. Monachon, J. Wu, and C. Dames, "Thermal diodes, regulators, and switches: Physical mechanisms and potential applications," *Appl. Phys. Rev.*, vol. 4, no. 4, Dec. 2017, Art. no. 041304, doi: 10.1063/1.5001072.

[22] B. Marland, D. Bugby, and C. Stouffer, "Development and testing of an advanced cryogenic thermal switch and cryogenic thermal switch test bed," *Cryogenics*, vol. 44, nos. 6–8, pp. 413–420, Jun. 2004, doi: 10.1016/j.cryogenics.2004.03.014.

[23] T. Yang *et al.*, "Millimeter-scale liquid metal droplet thermal switch," *Appl. Phys. Lett.*, vol. 112, no. 6, Feb. 2018, Art. no. 063505, doi: 10.1063/1.5013623.

[24] S.-H. Jeong, S.-K. Nam, W. Nakayama, and S.-K. Lee, "New design of a liquid bridge heat switch to ensure repetitive operation during changes in thermal conditions," *Appl. Thermal Eng.*, vol. 59, pp. 283–289, Sep. 2013, doi: 10.1016/j.applthermaleng.2013.05.027.

[25] K. E. Bulgrin, Y. S. Ju, G. P. Carman, and A. S. Lavine, "An investigation of a tunable magnetomechanical thermal switch," *J. Heat Transf.*, vol. 133, no. 10, pp. 1–7, Oct. 2011, doi: 10.1115/1.4004166.

[26] A. Ueno and Y. Suzuki, "Parylene-based active micro space radiator with thermal contact switch," *Appl. Phys. Lett.*, vol. 104, no. 9, pp. 1–5, 2014, doi: 10.1063/1.4867699.
[27] J. Yang *et al.*, "Enhanced and switchable nanoscale thermal conduction due to van der Waals interfaces," *Nature Nanotechnol.*, vol. 7, no. 2, pp. 91–95, Feb. 2012, doi: 10.1038/nnano.2011.216.
[28] M. Cleary, M. Hodes, R. Grimes, and M. T. North, "Design of a variable conductance heat pipe for a photonic component," in *ASME Int. Mech. Eng. Congr. Expo.*, 2006, pp. 1–10, doi: 10.1115/IMECE2006-13603.
[29] C. Melnick, M. Hodes, G. Ziskind, M. Cleary, and V. P. Manno, "Thermoelectric module-variable conductance heat pipe assemblies for reduced power temperature control," *IEEE Trans. Compon., Packag., Manuf. Technol.*, vol. 2, no. 3, pp. 474–482, Mar. 2012.
[30] M. J. Adams, M. Verosky, M. Zebarjadi, and J. P. Heremans, "High switching ratio variable-temperature solid-state thermal switch based on thermoelectric effects," *Int. J. Heat Mass Transf.*, vol. 134, pp. 114–118, May 2019, doi: 10.1016/j.ijheatmasstransfer.2018.12.154.
[31] M. Almanza, L. Depreux, F. Parrain, and M. LoBue, "Electrostatically actuated thermal switch device for caloric film," *Appl. Phys. Lett.*, vol. 112, no. 8, Feb. 2018, Art. no. 083901, doi: 10.1063/1.5009618.
[32] T. Avanessian and G. Hwang, "Thermal switch using controlled capillary transition in heterogeneous nanostructures," *Int. J. Heat Mass Transf.*, vol. 121, pp. 127–136, Jun. 2018, doi: 10.1016/j.ijheatmasstransfer.2017.12.142.
[33] H. Abouobaida and M. Cherkaoui, "New maximum power point tracker for fast changing environmental conditions," in *Proc. Int. Conf. Multimedia Comput. Syst.*, Apr. 2011, pp. 2401–2407, doi: 10.1109/ICMCS.2011.5945707.
[34] Y. S. Lim and J. H. Tang, "Experimental study on flicker emissions by photovoltaic systems on highly cloudy region: A case study in Malaysia," *Renew. Energy*, vol. 64, pp. 61–70, Apr. 2014, doi: 10.1016/j.renene.2013.10.043.
[35] L. M. Tolbert, B. Ozpineci, S. K. Islam, and F. Z. Peng, "Impact of SiC power electronic devices for hybrid electric vehicles," SAE Tech. Paper 2002-01-1904, USA, 2002, doi: 10.4271/2002-01-1904.
[36] A. R. McLanahan, C. D. Richards, and R. F. Richards, "A dielectric liquid contact thermal switch with electrowetting actuation," *J. Micromech. Microeng.*, vol. 21, no. 10, Oct. 2011, Art. no. 104009, doi: 10.1088/0960-1317/21/10/104009.
[37] M. Schweizer and J. W. Kolar, "Design and implementation of a highly efficient three-level T-type converter for low-voltage applications," *IEEE Trans. Power Electron.*, vol. 28, no. 2, pp. 899–907, Feb. 2013, doi: 10.1109/TPEL.2012.2203151.
[38] Z. Wang *et al.*, "A compact 250 kW silicon carbide MOSFET based three-level traction inverter for heavy equipment applications," in *Proc. IEEE Transp. Electrific. Conf. Expo (ITEC)*, Jun. 2018, pp. 212–216, doi: 10.1109/ITEC.2018.8450172.
[39] Y. Shi, L. Wang, R. Xie, Y. Shi, and H. Li, "A 60-kW 3-kW/kg five-level T-type SiC PV inverter with 99.2% peak efficiency," *IEEE Trans. Ind. Electron.*, vol. 64, no. 11, pp. 9144–9154, Nov. 2017, doi: 10.1109/TIE.2017.2701762.
[40] M. Che and S. Elbel, "Experimental study of local air-side heat transfer coefficient on real-scale heat exchanger fins by employing an absorption-based mass transfer method," *Appl. Thermal Eng.*, vol. 189, May 2021, Art. no. 116718, doi: 10.1016/j.applthermaleng.2021.116718.
[41] T. L. Bergman, A. S. Lavine, F. P. Incropera, and D. P. DeWitt, *Fundamentals of Heat and Mass Transfer*. Hoboken, NJ, USA: Wiley, 2011.
[42] *BERGQUIST SIL-PAD 400*, BERGQUIST, USA, 2018, p. 1.
[43] D. Huitink and A. Lucero, "Semi-empirical stress/energy-based acceleration of temperature cycling failure," in *Proc. IEEE Int. Rel. Phys. Symp.*, Apr. 2015, p. 4, doi: 10.1109/IRPS.2015.7112752.
[44] K. Wei, T. Cheng, D. D. C. Lu, Y. P. Siwakoti, and C. Zhang, "Multi-variable thermal modeling of power devices considering mutual coupling," *Appl. Sci.*, vol. 9, no. 16, pp. 1–15, 2019, doi: 10.3390/app9163240.
[45] E. C. W. de Jong, B. J. A. Ferreira, and P. Bauer, "Toward the next level of PCB usage in power electronic converters," *IEEE Trans. Power Electron.*, vol. 23, no. 6, pp. 3151–3163, Nov. 2008, doi: 10.1109/TPEL.2008.2004276.
[46] F. Blaabjerg, K. Ma, and D. Zhou, "Power electronics and reliability in renewable energy systems," in *Proc. IEEE Int. Symp. Ind. Electron.*, May 2012, pp. 19–30, doi: 10.1109/ISIE.2012.6237053.
[47] W. Lai, M. Chen, L. Ran, O. Alatise, S. Xu, and P. Mawby, "Low stress cycle effect in IGBT power module die-attach lifetime modeling," *IEEE Trans. Power Electron.*, vol. 31, no. 9, pp. 6575–6585, Sep. 2016, doi: 10.1109/TPEL.2015.2501540.
[48] *C2M0160120D Silicon Carbide Power MOSFET*, Cree, USA, 2015, pp. 1–10.
[49] C. Semini *et al.*, "Additive manufacturing for agile legged robots with hydraulic actuation," in *Proc. Int. Conf. Adv. Robot. (ICAR)*, Jul. 2015, pp. 123–129, doi: 10.1109/ICAR.2015.7251444.
[50] S. A. Merryman and D. K. Hall, "Chemical double-layer capacitor power source for electromechanical thrust vector control actuator," *J. Propuls. Power*, vol. 12, no. 1, pp. 89–94, Jan. 1996, doi: 10.2514/3.23995.
[51] M. Goldfarb, E. J. Barth, M. A. Gogola, and J. A. Wehrmeyer, "Design and energetic characterization of a liquid-propellant-powered actuator for self-powered robots," *IEEE/ASME Trans. Mechatronics*, vol. 8, no. 2, pp. 254–262, Jun. 2003, doi: 10.1109/TMECH.2003.812842.
[52] T. G. McGee, J. W. Raade, and H. Kazerooni, "Monopropellant-driven free piston hydraulic pump for mobile robotic systems," *J. Dyn. Syst., Meas., Control*, vol. 126, no. 1, pp. 75–81, Mar. 2004, doi: 10.1115/1.1649972.
[53] G. Qiao, G. Liu, Z. Shi, Y. Wang, S. Ma, and T. C. Lim, "A review of electromechanical actuators for more/all electric aircraft systems," *Proc. Inst. Mech. Eng., C, J. Mech. Eng. Sci.*, vol. 232, no. 22, pp. 4128–4151, Nov. 2018, doi: 10.1177/0954406217749869.
[54] J. Rahmer, C. Stehning, and B. Gleich, "Remote magnetic actuation using a clinical scale system," *PLoS ONE*, vol. 13, no. 3, pp. 1–19, 2018, doi: 10.1371/journal.pone.0193546.
[55] Z. Yang and L. Zhang, "Magnetic actuation systems for miniature robots: A review," *Adv. Intell. Syst.*, vol. 2, no. 9, Sep. 2020, Art. no. 2000082, doi: 10.1002/aisy.202000082.
[56] S. John, A. Chaudhuri, and N. M. Wereley, "A magnetorheological actuation system: Test and model," *Smart Mater. Struct.*, vol. 17, no. 2, Apr. 2008, Art. no. 025023, doi: 10.1088/0964-1726/17/2/025023.
[57] T. Yang, P. V. Braun, N. Miljkovic, and W. P. King, "Phase change material heat sink for transient cooling of high-power devices," *Int. J. Heat Mass Transf.*, vol. 170, May 2021, Art. no. 121033, doi: 10.1016/j.ijheatmasstransfer.2021.121033.
[58] T. Yang *et al.*, "A composite phase change material thermal buffer based on porous metal foam and low-melting-temperature metal alloy," *Appl. Phys. Lett.*, vol. 116, no. 7, Feb. 2020, Art. no. 071901, doi: 10.1063/1.5135568.

Tianyu Yang received the B.S. degree in engineering mechanics and aerospace engineering from Tsinghua University, Beijing, China, in 2016, and the Ph.D. degree in mechanical engineering from the Department of Mechanical Science and Engineering, University of Illinois at Urbana–Champaign, Urbana, IL, USA, in 2021.

Her research interests are thermal management techniques to control temperature uniformity and cooling capacity by applying thermal switches and phase change materials.

Fei Diao (Graduate Student Member, IEEE) received the B.E. and M.E. degrees in electrical engineering from Southwest Jiaotong University, Chengdu, China, in 2015 and 2018, respectively. He is currently pursuing the Ph.D. degree in electrical engineering with the Department of Electrical Engineering, University of Arkansas, Fayetteville, AR, USA.

In 2020 and 2021, he was a Summer Intern with Eaton Corporation, Menomonee Falls, WI, USA. He currently works with John Deere, Cary, NC, USA. His main research interests include modulation and control of power converters, and wide bandgap (WBG) power device applications.

H. Alan Mantooth (Fellow, IEEE) received the B.S.E.E. and M.S.E.E. degrees from the University of Arkansas (UA), Fayetteville, AR, USA, in 1985 and 1986, respectively, and the Ph.D. degree from the Georgia Institute of Technology (Georgia Tech), Atlanta, GA, USA, in 1990.

He then joined Analogy, a startup company in Oregon, where he focused on semiconductor device modeling and research and development of modeling tools and techniques. In 1998, he joined the Department of Electrical Engineering, UA, where he currently holds the rank of a Distinguished Professor. His current research interests include analog and mixed-signal IC design and CAD, semiconductor device modeling, power electronics, power electronics packaging, and cybersecurity. He helped to establish the National Center for Reliable Electric Power Transmission (NCREPT), UA, in 2005. He serves as the Executive Director of NCREPT as well as two of its centers of excellence: the NSF Industry/University Cooperative Research Center on GRid-connected Advanced Power Electronic Systems (GRAPES) and the Cybersecurity Center on Secure, Evolvable Energy Delivery Systems (SEEDS) funded by the U.S. Department of Energy. In 2015, he also helped to establish the UA's first NSF Engineering Research Center entitled Power Optimization for Electro-Thermal Systems (POETS) that focuses on high power density systems for electrified transportation applications. He has co-founded three companies in design automation (Lynguent), Fayetteville; IC design (Ozark Integrated Circuits), Fayetteville; and cybersecurity (Bastazo), Fayetteville; as well as advising a fourth in power electronics packaging (Arkansas Power Electronics International), Fayetteville; to maturity and acquisition as a Board Member.

Dr. Mantooth is a member of Tau Beta Pi, Sigma Xi, and Eta Kappa Nu; and a Registered Professional Engineer in Arkansas. He holds the 21st Century Research Leadership Chair in Engineering. He serves as the Senior Past-President for the IEEE Power Electronics Society and the Editor-in-Chief for the IEEE OPEN JOURNAL OF POWER ELECTRONICS.

Yue Zhao (Senior Member, IEEE) received the B.S. degree in electrical engineering from the Beijing University of Aeronautics and Astronautics, Beijing, China, in 2010, and the Ph.D. degree in electrical engineering from the University of Nebraska–Lincoln, Lincoln, NE, USA, in 2014.

He was an Assistant Professor with the Department of Electrical and Computer Engineering, Virginia Commonwealth University, Richmond, VA, USA, from 2014 to 2015. Since August 2015, he has been with the University of Arkansas (UA), Fayetteville, AR, USA, where he is currently an Associate Professor with the Department of Electrical Engineering. He also serves as the Site Director of the National Science Foundation (NSF) Center on GRid-connected Advanced Power Electronic Systems (GRAPES). He has four U.S. patents granted and coauthored more than 100 papers in refereed journals and international conference proceedings. His current research interests include electric machines and drives, power electronics, and renewable energy systems.

Dr. Zhao was a recipient of the 2018 NSF CAREER Award, the 2020 IEEE Industry Applications Society Andrew W. Smith Outstanding Young Member Achievement Award, and the 2020 UA College of Engineering Dean's Award of Excellence. He is an Associate Editor of the IEEE TRANSACTIONS ON INDUSTRY APPLICATIONS and IEEE OPEN JOURNAL OF POWER ELECTRONICS.

William P. King (Fellow, IEEE) received the Ph.D. degree from Stanford University, Stanford, CA, USA, in 2002.

He has completed the Program for Leadership Development at the Harvard Business School, Boston, MA, USA. He is currently the Ralph A. Andersen Endowed Chair of the Department of Mechanical Science and Engineering, University of Illinois at Urbana–Champaign, Urbana, IL, USA, where he also holds courtesy appointments at the Department of Electrical and Computer Engineering and the Department of Materials Science and Engineering. He was the founding Chief Technology Officer of the Digital Manufacturing and Design Innovation Institute (DMDII), UI LABS, Chicago, IL, USA. DMDII is one of the first institutes in the U.S. National Network for Manufacturing Innovation. His research focuses on advanced manufacturing, nanotechnology, heat transfer, and advanced materials.

Dr. King is a fellow of American Society of Mechanical Engineers (ASME), American Association for the Advancement of Science (AAAS), American Physical Society (APS), and Society of Manufacturing Engineers (SME). He was a winner of multiple awards, including the ASME Gustus-Larson Award for accomplishment in mechanical engineering.

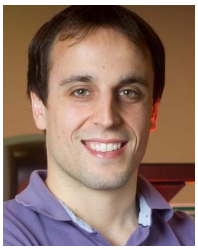

Nenad Miljkovic (Member, IEEE) received the B.A.Sc. degree in mechanical engineering from the University of Waterloo, Waterloo, ON, Canada, in 2009, and the M.S. and Ph.D. degrees in mechanical engineering from the Massachusetts Institute of Technology, Cambridge, MA, USA, in 2011 and 2013, respectively.

He is currently an Associate Professor of mechanical science and engineering with the University of Illinois at Urbana–Champaign, Urbana, IL, USA, where he leads the Energy Transport Research Laboratory and co-directs the Air Conditioning and Refrigeration Center. He has courtesy appointments at the Department of Electrical and Computer Engineering and the Materials Research Laboratory, University of Illinois at Urbana–Champaign. His group's research intersects the multidisciplinary fields of thermo-fluid science, interfacial phenomena, and renewable energy.

Dr. Miljkovic is a fellow of American Society of Mechanical Engineers (ASME). He was a recipient of the National Science Foundation CAREER Award, the American Chemical Society Petroleum Research Fund Doctoral New Investigator Award, the Office of Naval Research Young Investigator Award, the ASME Pi Tau Sigma Gold Medal, and the Bergles-Rohsenow Young Investigator Awards.